APPLIED SCIENCES AND ENGINEERING

Origins of the large piezoelectric response of samarium-doped lead magnesium niobate–lead titanate ceramics

Matija Arzenšek[1]†, Urh Toš[1], Silvo Drnovšek[1], Mirela Dragomir[1], Hana Uršič[1], Mojca Otoničar[1], Paulius Jankauskas[2], Šarūnas Svirskas[2], Tadej Rojac[1]*

The recent discovery of the large piezoelectric response of $Pb(Mg_{1/3}Nb_{2/3})O_3$-$PbTiO_3$ (PMN-PT) ceramics induced by samarium doping has provided a substantially improved functionality to the group of lead-based relaxor-ferroelectric materials. Different mechanisms have been so far proposed for the large piezoelectricity; however, the explanations are contradictory and focused on a unified description. Here, we use nonlinear harmonic piezoelectric measurements combined with multiscale structural analysis to clarify the origins of the ultrahigh piezoelectric response of samarium-doped PMN-PT. Our methodological approach allowed us to separate the multiple piezoelectric contributions, revealing their quantitative role in the total response. The results show that the ultrahigh piezoelectricity cannot be attributed to a single mechanism but is rather a complex combination of different contributions originating from the multiple effects of samarium doping on the long- and short-range structure of PMN-PT. The study offers a baseline for future engineering of the key material parameters affecting the large piezoelectric response of relaxor-ferroelectric ceramics.

INTRODUCTION

Owing to their exceptional dielectric and piezoelectric properties, relaxor ferroelectrics based on lead perovskites, such as $Pb(Mg_{1/3}Nb_{2/3})O_3$-$xPbTiO_3$ (PMN-xPT where x is in mol %), are attractive for numerous applications, including capacitive energy storage (1), actuators (2), electrocalorics (3), piezoelectric transducers (4), energy harvesting (5), and electro-optic devices (6). Despite their excellent functionality, these materials have been a real brainteaser for the research community. The main reason is their complex nanopolar structure, which has been under debate for decades, and in many aspects, it is still unclear (7–15). An important milestone was recently achieved by Li *et al.* (16), reporting the discovery of extraordinary piezoelectric properties of PMN-PT ceramics by doping with samarium (Sm) ions. The reported longitudinal piezoelectric d_{33} coefficient of ~1500 pC/N for the PMN-29PT composition doped with 2.5% Sm is not only doubled with respect to the coefficient of undoped PMN-PT [d_{33} ~ 700 pC/N for PMN-35PT (17)] but also exceeds by far the performance of commercial soft $Pb(Zr,Ti)O_3$ (PZT) ceramics (16). Impressively, the ultrahigh response of Sm-doped PMN-PT ceramics even reached the level of piezoelectric activity typical for undoped morphotropic PMN-PT single crystals (18).

The obvious question that arises following the discovery of Sm-doped PMN-PT ceramics is: What is the origin of the large piezoelectric response? The question relates to the structural consequences of the incorporation of Sm dopant into the A site of the perovskite, considering that among the series of rare-earth dopants that were tested experimentally (i.e., La, Nd, Sm, Gd, Dy, and Y), Sm doping results in the largest effect on the piezoelectricity of PMN-PT

ceramics (19). In that study, the strongest effect of Sm in enhancing the piezoelectric and dielectric response, relative to the undoped ceramics, was attributed to its capability of inducing the largest local strain distortion considering that Sm^{3+} is the smallest rare-earth cation among the dopant series tested that still prefers to be incorporated into the A sites of the perovskite, replacing Pb^{2+} ions. A pronounced effect in enhancing the piezoelectric response was also observed for the Eu dopant (20), which appears reasonable considering that Eu and Sm occupy neighboring positions in the lanthanide series. Being at the crossover between A and B site substituents, literature data indicate that, in $Pb(Ni_{1/3}Nb_{2/3})O_3$-$Pb(Zr,Ti)O_3$ (PNN-PZT) ceramics, the Sm^{3+} cations can be incorporated into either A site (21) or B site (22), apparently leading to softening or hardening behavior, respectively.

Originally, the large response of Sm-doped PMN-PT was attributed to the polarization rotation under applied external electric (or mechanical) fields (16). This is expected as polarization rotation is the lattice contribution (often referred to as the intrinsic effect) that is extensively used to explain the maximum in the electromechanical properties of PMN-PT and similar lead-based perovskite ceramics and single crystals close to their morphotropic phase boundary (MPB) compositions (23–25). The additional aspect of the mechanism originally proposed by Li *et al.* (16), however, is that the polarization rotation is facilitated by the presence of dynamic polar nanoregions (PNRs), residing inside the ferroelectric matrix, which arise as a result of local structural heterogeneities induced by the Sm dopant. This local polar picture was supported by phase-field modeling and was linked to a relaxation in the dielectric and piezoelectric coefficients, experimentally observed at cryogenic temperatures. The mechanism is an extended version of a previously reported model that attempts to explain the role of PNRs on the field-induced polarization rotation in undoped PMN-PT and similar relaxor-PT single crystals (26).

The explanation based on polarization rotation interacting with PNRs was soon questioned by Shepley *et al.* (27) who presented

[1]Electronic Ceramics Department, Jožef Stefan Institute, Jamova cesta 39, 1000 Ljubljana, Slovenia. [2]Faculty of Physics, Vilnius University, Saulėtekio al. 3, 10257 Vilnius, Lithuania.
*Corresponding author. Email: tadej.rojac@ijs.si
†Present address: Impol Aluminium Industry, Partizanska 38, 2310 Slovenska Bistrica, Slovenia.

solid experimental evidences that the cryogenic relaxation in the dielectric response of a series of PIN-PMN-PT [where PIN is Pb(In$_{1/2}$Nb$_{1/2}$)O$_3$] relaxor-ferroelectric ceramics and single crystals is not consistent with the PNR freezing phenomenon. Instead, the data suggested a thermally activated process, raising further uncertainties in the model based on polarization rotation. To fill in the gap, a thermodynamic framework was developed, hypothesizing that, in domain-engineered single crystals, the polarization rotation occurs inside static domain walls (DWs) of Néel type, leading to domain wall broadening under applied fields, rather than classical domain wall translation (28). While interesting as a concept, the model still lacks of experimental validations alongside the elaboration of multiple shortcomings associated with the simplifications used in the model [details are discussed by Bell *et al.* (28)]. On the other hand, the apparent thermally activated polarization rotation is compatible with a recent structural picture elaborated using in situ x-ray diffraction (XRD) and total scattering experiments combined with reverse Monte Carlo simulations (29). In that study, it was proposed that the large piezoelectric response of 2.5% Sm-doped PMN-29PT lies in the polarization rotation inside an average tetragonal phase where the ease of rotation is attributed to the thermally induced local monoclinic structure with polar axis pointing away from the average tetragonal direction. This picture is, in its nature, consistent with that proposed by Li *et al.* (16, 26); however, the local symmetry and the thermal relaxation of the local polar structures appear different. To be also noted is that none of the provided explanations discuss the possible role of Sm doping on the dynamics of so-called low-angle DWs, recently shown to play a dominant role in the piezoelectric response of undoped monoclinic PMN-PT ceramics exhibiting pronounced relaxor character (30).

Additional uncertainties regarding the true origin of the large response of Sm-doped PMN-PT ceramics has recently been presented by Li *et al.* (31). In contrast to the increased heterogeneities by Sm doping as the origin of the enhanced response (16), Li *et al.* (31) suggested that the reason lies in the softening effects provoked by donor doping, i.e., by Sm^{3+} ions replacing Pb^{2+} ions on the A site. The explanation is similar in nature to that known for donor-doped soft Pb(Zr,Ti)O$_3$ (PZT) (32) with the additional possibility that the reduced oxygen vacancy concentration by donor doping could possibly affect the mobility of PNRs [as proposed earlier (33)], making polarization rotation easier. This idea is in contradiction with the recent study by Kumar *et al.* (34) who stated that Sm doping, instead, increases the oxygen vacancy concentration due to the reduction of Sm^{3+} to Sm^{2+} states during ceramic sintering, leading to an increased electrical conductivity of the ceramics after Sm doping. Clearly, the increased electrical conductivity after Sm doping experimentally observed by Kumar *et al.* (34) is in contradiction with the decreased conductivity reported in the study by Li *et al.* (31). Nevertheless, it must be pointed out that the reduction of lanthanides from Ln^{3+} to Ln^{2+} states requires, in general, strong reducing agents. For example, with some exceptions, experiments and thermodynamic considerations show that lanthanide monoxides, such as SmO, cannot be prepared in the solid state (35). Considering the only known, isolated case of Sm^{2+} stabilized in crystalline SrB$_4$O$_7$ and the inability of Sm^{3+} to reduce in a structural environment with Pb ions (case of PbB$_4$O$_7$), it is reasonable to think that Sm^{2+} reduced ions are unlikely to form in Sm-doped PMN-PT, unless the annealing is performed under severe reducing conditions. Therefore, the increased electrical conductivity of PMN-PT after

doping with Sm (34) must necessarily be explained in a different context, possibly by considering alternative dopant-charge compensation schemes.

Despite the recent progress made in the understanding of the piezoelectricity of Sm-doped PMN-PT, which is of vital importance for the development of performant piezoelectrics, the current state-of-the-art is based on explanations that are often contradictory and insufficient to explain all the aspects of the Sm-induced piezoelectric enhancement. Instead of concentrating on a single explanation, in the present study, the strategy is to consider and critically combine all of them in a coherent picture. To achieve this objective, we performed nonlinear harmonic analysis of the converse piezoelectric response of PMN-29PT doped with 0 to 3% Sm. The analysis enabled us to deconvolute the total piezoelectric response and examine its individual contributions. On the basis of the analysis of the domain structure, phase composition, and atomic-scale polar displacements, we examine the involvement of the possible dynamic mechanisms within each of the extracted piezoelectric contributions. The results confirm that none of the individually reported mechanisms can explain the presented experimental data in its entirety. A consistent picture is determined by considering the multiple effects of the Sm dopant, including those associated with the average and local structure, domain configuration, structural disorder of relaxor origins, donor-related softening, and critical temperatures of the PMN-PT material system.

RESULTS

Analysis of the nonlinear piezoelectric response

To separate the different contributions to the large piezoelectric response of Sm-doped PMN-PT, we first explain the multiple effects of Sm doping on the characteristic temperatures and relaxor features. This is performed by comparing the phase diagrams of undoped and 3% Sm-doped PMN-xPT in Fig. 1A. The phase diagrams were constructed based on the temperature-dependent dielectric permittivity analysis (details are explained in supplementary material 1). Introduction of Sm dopant into the perovskite leads to three main effects: (i) a compositional shift of the monoclinic-to-tetragonal (M-to-T) MPB toward the relaxor PMN end-member, i.e., from PMN-35PT (undoped) to the PMN-29PT (doped) composition (see arrow A in Fig. 1A); (ii) an increased relaxor-like disorder at the MPB composition, evidenced from the increased difference in the temperature of permittivity maximum (T_m) measured at different frequencies (follow arrows connecting point B); and (iii) a decreased freezing temperature T_f (arrow C). Therefore, the MPB composition in the doped system differs from the MPB composition in the undoped system specifically by showing a stronger relaxor disorder and lowered T_f (compare doped PMN-29PT with undoped PMN-35PT in the phase diagrams).

Focusing on the most interesting composition, PMN-29PT, we present in Fig. 1B the temperature dependence of the dielectric permittivity ε' as it evolves with increasing Sm concentration. The dielectric behavior of all the analyzed samples is characterized by the frequency-dispersive permittivity maximum, T_m, which is preceded by a weaker and frequency-independent peak. The latter is associated with the M-to-T phase transition, noted here as T_{tetr}. Note that the MPBs in the PMN-PT system are curved and thus have a polymorphic character (36) (in this context and assuming that the curved MPB nature is preserved by Sm doping, in this study, T_{tetr}

will be often used synonymously with MPB). Besides the shift of all the ε' peaks to lower temperatures with increasing Sm concentration, the other obvious consequence of Sm doping is the pronounced broadening and increased frequency dispersion of the dielectric maximum (T_m). The characteristic temperatures (T_m, T_f, and T_{tetr}) and the temperature difference of T_m measured at 1 and 100 kHz (ΔT_m), which is commonly used to quantify the relaxor signature of a material, are collected in Fig. 1C. To be noted is that the freezing temperature T_f values were determined by the analysis of the derivative of the dielectric permittivity, showing good agreement with the T_f values determined by conventional Vogel-Fulcher fitting

(for details, see supplementary material 1). The data shown in Fig. 1C confirm a substantial decrease in the characteristic temperatures (gray area of the graph) alongside the enhanced relaxor disorder by Sm doping (green area of the graph). The results are consistent with a great number of recent reports on Sm-doped PMN-PT and PMN-PZN-PT ceramics [PZN is Pb(Zn$_{1/3}$Nb$_{2/3}$)O$_3$] [16, 34, 37–43]. The same trend was observed in PMN-PT upon Eu doping [20, 44, 45].

We continue the analysis on PMN-29PT by presenting in Fig. 2A the electric field dependence of the converse longitudinal piezoelectric d'_{33} coefficient. A notable increase in the coefficient is observed by Sm doping across the entire measured field range, especially at
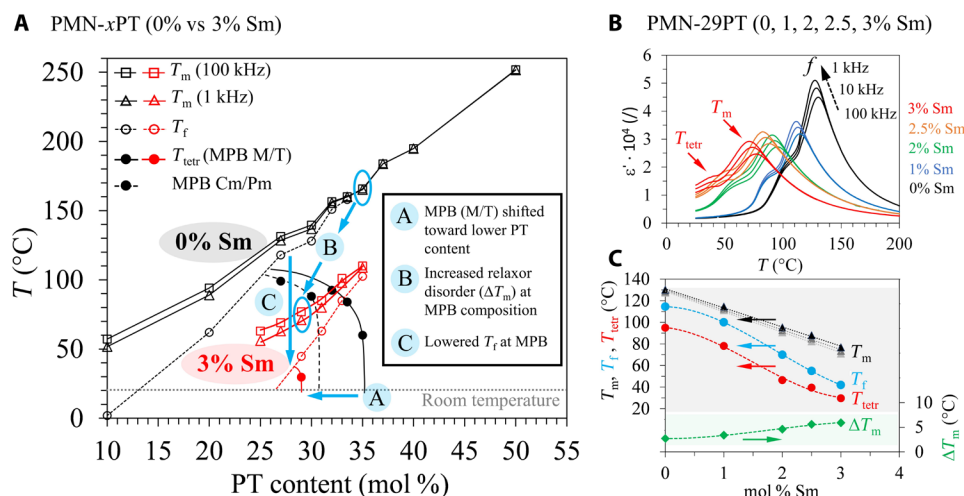

Fig. 1. Effects of Sm doping on characteristic temperatures and relaxor features of PMN-PT. (**A**) Phase diagram of undoped (black) and 3 mol % Sm-doped (red) PMN-PT highlighting the effects of Sm doping (arrows A, B, and C). T_m, T_f, and T_{tetr} denote the temperature of the frequency-dispersive maximum in the dielectric permittivity, freezing temperature, and M-to-T phase transition temperature, respectively. The two known MPBs between M and T phases and between two M phases (space group Cm and Pm) for the undoped system are also noted. Data for T_m are shown for frequencies of 1 and 100 kHz. The phase diagrams were constructed based on the analysis of the temperature-dependent dielectric permittivity [the data for the undoped system are reported in (52)]. (**B**) Temperature dependence of dielectric permittivity (ε') measured at 1, 10, and 100 kHz during heating of PMN-29PT samples doped with 0 to 3 mol % Sm (T_m and T_{tetr} are noted). (**C**) Characteristic temperatures (T_m, T_f, and T_{tetr}) and difference between T_m measured at 1 and 100 kHz (ΔT_m) as a function of Sm doping concentration, as extracted from the data shown in (B).
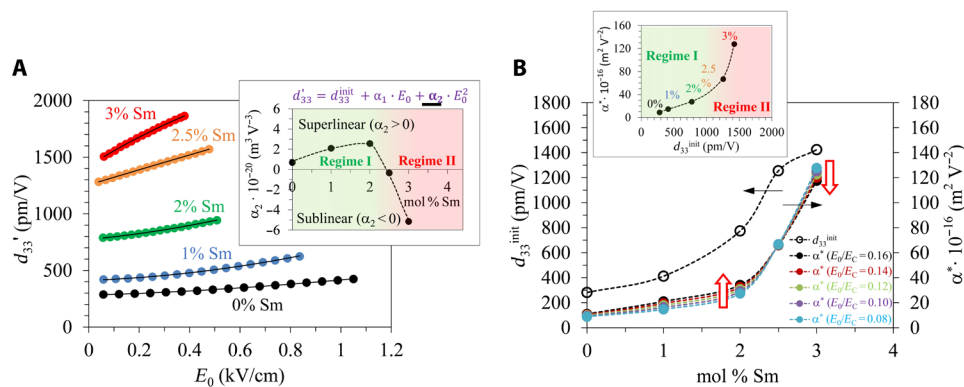

Fig. 2. Nonlinear piezoelectric response of PMN-29PT doped with 0 to 3% Sm measured at room temperature. (**A**) Converse piezoelectric d'_{33} coefficient as a function of the electric field amplitude E_0 in undoped and Sm-doped PMN-29PT. Each set of data was fitted with a second-order polynomial function. The corresponding equation and the resulting quadratic coefficient α_2 plotted versus Sm concentration are shown in the inset. On the basis of the change of sign of α_2, two nonlinear regimes are identified (marked in green as regime I and in red as regime II). (**B**) Reversible d_{33}^{init} and irreversible α^* Rayleigh coefficients as a function of Sm concentration. The irreversible α^* coefficient is considered field-dependent and is plotted for different relative fields E_0/E_C where E_C is the coercive field. The two red arrows indicate the field-dependent trend of α^*, marking the superlinearity (upward arrow; α^* increases with E/E_C) and sublinearity (downward arrow; α^* decreases with E/E_C), in line with the data shown in (A). The inset plots α^* versus d_{33}^{init} for each composition with the two nonlinear regimes marked.

dopant concentrations exceeding 2%. The comparison of d'_{33} measured at the highest electric field revealed an almost 500% increase in the coefficient, i.e., from ~420 pm/V for undoped to ~1900 pm/V for 3% doped. The small-signal d'_{33} values for the 3%-doped sample (i.e., 1500 to 1900 pm/V for driving fields of 0.06 to 0.38 kV/cm) are among the highest reported for similar ceramic compositions (*16*, *19*, *29*, *31*, *34*, *39*, *46*, *47*). This confirms the ceramic quality and an efficient incorporation of Sm into the perovskite lattice (structural and microstructural data for the PMN-29PT series are presented in supplementary material 2).

In addition to the piezoelectric enhancement, Sm doping also induces qualitative changes in the nonlinear response. This can be observed in Fig. 2A where the transition is traced from an upcurved (superlinear) d'_{33} field dependence (see trendlines from 0 to 2% Sm) to a linear dependence (2.5% Sm), followed by a saturating-like (sublinear) behavior (3% Sm). A quantitative picture of this transition is demonstrated by plotting the quadratic coefficient of the second-order polynomial (α_2) fitted to the $d'_{33} - E_0$ experimental data (inset of Fig. 2A). The positive α_2 coefficient first increases in the superlinear regime up to 2% Sm ($\alpha_2 > 0$; green area) then changes sign, marking the transition to a sublinear regime ($\alpha_2 < 0$; red area). The main result of this analysis is the identification of two distinct nonlinear regimes denoted here and in the following as regimes I and II (inset of Fig. 2A).

In the next step, we separate the reversible (R; d_{33}^{init}) and irreversible (IR; α^*) contributions from the total piezoelectric response, plotting them as a function of Sm concentration in Fig. 2B. The α^* coefficient is displayed for different relative driving electric fields, represented by E_0/E_C where E_C is the coercive field determined from polarization–electric field (P-E) hysteresis loops (supplementary material 3). The two contributions were separated using Rayleigh law (RL) analysis [details are reported in supplementary material 4 and (*30*)]. To remind the reader, we note that, in macroscopic terms, the intercept of the $d'_{33} - E_0$ curve at $E_0 = 0$, i.e., the d_{33}^{init} coefficient, includes both lattice and R nonlattice contributions, while the field-dependent slope of the $d'_{33} - E_0$ relation, i.e., α^*, includes IR nonlattice contributions. The lattice contribution is, in principle, associated with ion displacements under applied external field within individual domains and is often referred to as the intrinsic effect. On the other hand, nonlattice contributions, often referred to as the extrinsic effects, are, in most cases, shown or assumed to be dominated by dynamics of DWs and/or interface boundaries (*48*, *49*). As shown in Fig. 2B, both d_{33}^{init} and α^* increase with Sm addition, confirming that Sm doping enhances both lattice and nonlattice responses to external field, similarly as was reported for the Sm-doped PMN-PZT system (*50*). The most important observation is that the influence of Sm doping on the two coefficients is not the same. For example, d_{33}^{init} increases progressively with Sm addition until saturation at 3% Sm, whereas α^* shows a slight increase up to 2% Sm (16% of the total change of α^*), followed by an abrupt increase above this concentration level (84% of the total change of α^*). Note that this large increase in α^* in the upper range of the Sm concentration is coincident with the superlinear-to-sublinear field dependency transition (see upward and downward red arrows in Fig. 2B). The decoupling between the R and IR contributions as a function of the dopant concentration is displayed in the inset of Fig. 2B where α^* is plotted against d_{33}^{init}. The curve demonstrates a break of slope between 2 and 2.5% Sm, marking the transitional point between the two nonlinear regimes I and II, which were also consistently

identified in the total d'_{33}-versus-E_0 piezoelectric response (inset of Fig. 2A).

In the search of the origins of the two nonlinear regimes observed with Sm doping, we performed harmonic analysis of the piezoelectric response, a method particularly useful in the evaluation of nonlattice contributions, such as DW dynamics (*30*, *51*). To extract comprehensive information, we combine the first harmonic (Fig. 3A), third harmonic (Fig. 3B), and total piezoelectric response (Fig. 3C). As reported in our previous studies (*30*, *52*), the analysis considers RL in a way that the predicted first and third harmonic components in the Fourier expansion of RL relations are used as a reference [Fourier series analysis of RL is reported in supplementary material 4 and (*30*)]. These reference points, to which the experimental data are compared in the following steps, are represented by the red dashed line in Fig. 3A (RL line) and red triangular region in Fig. 3B (see hysteresis schematic in red).

We first evaluate the harmonic response of undoped PMN-29PT by referencing our previous study on the undoped PMN-PT system (*30*, *52*). Figure 3A shows the ratio of the hysteretic-to-nonlinear fractional contributions $\left(\frac{\Delta d''_{33}}{\Delta d'_{33}} \right)$ determined by fitting the experimental $\Delta d''_{33}$ versus $\Delta d'_{33}$ datasets (supplementary material 5). By inspecting the undoped sample, it can be observed that the $\frac{\Delta d''_{33}}{\Delta d'_{33}}$ ratio (0.73) is notably higher than predicted by RL (~0.42). This is reflected in a much larger experimental hysteresis area when compared to the area predicted by RL (88% relative difference as shown in Fig. 3C). At the same time, the third harmonic response of the undoped sample shows a strong divergent-like anhysteretic component with the third harmonic phase angle δ_3 evolving with driving field toward $\delta_3 = -116°$ (black arrow in Fig. 3B, green area). These two components of the nonlinear response, i.e., hysteretic IR (Fig. 3A) and anhysteretic R (Fig. 3B), show non-RL characteristics and were previously linked to the dynamic displacements of so-called low-angle DWs (*30*, *52*).

Recent research has provided valuable insights into the complex origins of low-angle DWs, suggesting links to the local structural disorder present in PMN-based relaxor materials (*10*, *12*, *13*). In agreement with these structural studies, it was recently found that the field-induced response of low-angle DWs dominates the piezoelectric nonlinearity of undoped monoclinic PMN-*x*PT compositions ($20 < x < 32$) with relaxor features (*30*). In particular, the large hysteretic IR response (as also identified here for the undoped PMN-29PT) was proposed to originate from a cascade-like DW switching (*53*). On the other hand, the origin of the anhysteretic R DW motion (green area in Fig. 3B) is not entirely clear. Such dynamics could be related to the presence of nanodomains whose reversible switching at weak fields would be a consequence of the stress-accommodating state at zero field, similarly as discussed for shape memory effects in martensite alloys (*54*). The tendency for DWs in poled PMN-PT crystals to move reversibly was also directly visualized by in situ transmission electron microscopy (TEM) (*55*).

After identifying the low-angle DW dynamic contribution to the R and IR nonlinearity of undoped PMN-29PT, we have now the basis to investigate the effect of Sm doping. Using the same subdivision of the nonlinear response into two regimes, as presented earlier in Fig. 2, we can extract two observations for regime I: (i) an increased $\frac{\Delta d''_{33}}{\Delta d'_{33}}$ ratio with Sm addition with a maximum of 0.81 observed at 1% Sm (Fig. 3A, see green arrow) and (ii) a simultaneous enhancement of the divergent-like third harmonic component (Fig. 3B, follow the
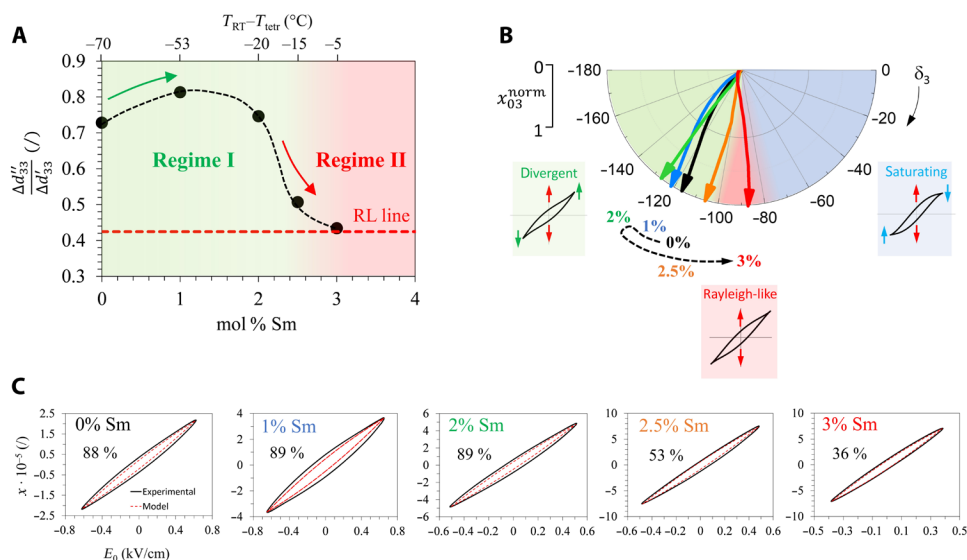
Fig. 3. Piezoelectric harmonic analysis of PMN-29PT doped with 0 to 3% Sm. (**A**) Ratio of the hysteretic-to-nonlinear fractional contributions $\frac{\Delta d''_{33}}{\Delta d'_{33}}$ as a function of Sm concentration. The red dashed line denotes the $\frac{\Delta d''_{33}}{\Delta d'_{33}}$ ratio of $\frac{4}{3\pi} \sim 0.42$ predicted by RL. The upper axis in the graph represents the proximity of the temperature of the tetragonal phase transition (T_{tetr}) to room temperature (T_{RT}-T_π) corresponding to each Sm concentration (T_{tetr} values are given in Fig. 1C). The green arrow illustrates the increasing trend of the $\frac{\Delta d''_{33}}{\Delta d'_{33}}$ ratio in the nonlinear regime up to 2% Sm (regime I, green), while the red arrow shows the transition to RL-like behavior in the nonlinear regime above 2% Sm (regime II, red). (**B**) Phasor diagram showing the evolution of the third harmonic phase angle δ_3 with increasing electric field amplitude for PMN-29PT ceramic samples (data are shown as a function of normalized third harmonic strain amplitude, x^{norm}_{03}). The phasors are color-coded according to the Sm concentration (see legend below the phasor diagram). Colored regions in the phasor diagram correspond to different ranges of δ_3 values causing a particular type of hysteresis loop deformation (see hysteresis loop schematics): (i) divergent-like (green), (ii) RL-like (red), and (iii) saturating-like (blue) deformation. The dashed arrow below the diagram illustrates the enhanced divergent-like response up to 2% Sm, followed by the transition to the RL-like behavior above 2% Sm ($\delta_3 \sim -90°$). (**C**) Piezoelectric hysteresis loops of PMN-29PT sample series where black are experimental and red are RL-calculated hysteresis loops. The values in the graphs corresponds to the observed relative differences between experimental and calculated hysteresis areas.

dashed line from 0 to 2% Sm). Additional support to this behavior is provided by the piezoelectric phase angle and the in-phase third harmonic strain as they evolve with electric field and Sm concentration (supplementary material 6). By assuming that the underlying mechanisms remain the same, we can conclude for regime I that both the hysteretic IR and the anhysteretic R dynamic contribution of low-angle DWs are enhanced by Sm doping. This is consistent with the enhanced frequency dispersion of the permittivity maximum as Sm is introduced in the perovskite (Fig. 1C, see ΔT_m). Considering the nonlinear parameters discussed in Fig. 3 (A and B), the effect of Sm doping in regime I is qualitatively similar to the effect of lowering the PT content in undoped PMN-PT where the system approaches the relaxor PMN end-member (*30*, *52*).

At doping concentration above 2% Sm, in regime II, the nonlinear response exhibits a qualitative change to an RL-like response where $\frac{\Delta d''_{33}}{\Delta d'_{33}}$ and δ_3 reach values closer to those predicted by RL relations (Fig. 3, A and B). This is also reflected in the hysteresis loop showing a much better fit to the RL hysteresis (although 36% discrepancy in the hysteresis area of the 3%-doped sample is still observed in Fig. 3C, which will be discussed on a later stage). Qualitatively, exactly the same transition to an RL-like response was reported in another study for undoped PMN-PT and donor-doped PZT near respective MPBs with the tetragonal phase (*30*, *52*). Similarly, the best match between the experimental polarization hysteresis loop and the RL-predicted loop was also observed for MPB compositions in Sm-doped PMN-PT-PSN [PSN is Pb($Sc_{1/2}Nb_{1/2}$)

O_3] (*56*). By combining our results, we can also identify an apparent correlation between the nonlinear transition to regime II and the onset of the tetragonal phase; in fact, regime II can be roughly set within a proximity of ~15°C to T_{tetr} (see upper axis plotting T_{RT}-T_{tetr} in Fig. 3A). The results therefore indicate that the transition to an RL-like nonlinear response could be related to the appearance of the tetragonality and, as such, it is a secondary phenomenon induced by Sm. This is consistent with recent theoretical and experimental studies suggesting that Sm doping in PMN-PT induces a tetragonal-like lattice distortion on a short structural range (*19*, *57*), which, above a critical Sm concentration, develops into a long-range (average) tetragonal phase (*16*, *29*, *31*, *34*). In the following, we examine the hypothetical link between the RL-like nonlinear response and tetragonal phase by characterizing the domain structure and phase composition of the undoped and doped PMN-29PT ceramics.

Domain configuration, phase composition, and atomic structure

Piezoresponse force microscopy (PFM) images (Fig. 4A) reveal a complex and nonmonotonous development of the domain structure in PMN-29PT with increasing Sm concentration, closely corresponding to the observed transition in the piezoelectric properties. The domain structure of undoped sample (0% Sm) is characterized by wedge-shaped domains, already observed in similar PMN-PT ceramic compositions (*58*). Note also that the average symmetry of PMN-29PT, as identified by Rietveld refinement of the XRD pattern
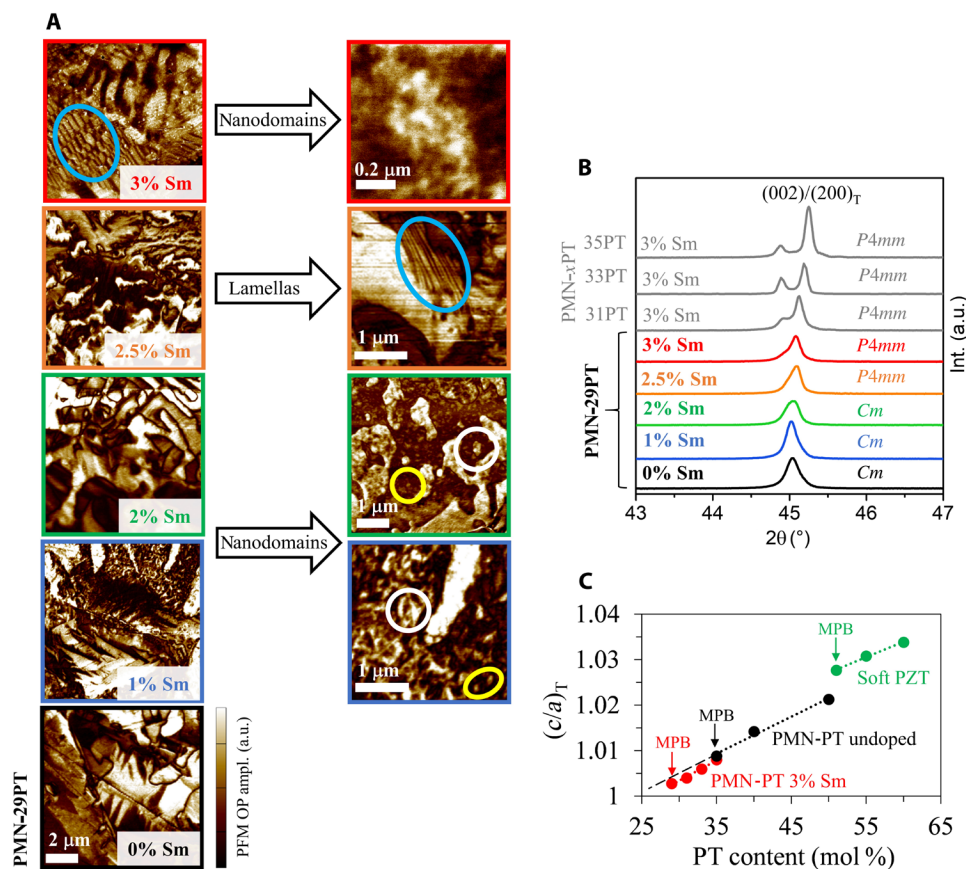
Fig. 4. Evolution of domain structure and phase composition in PMN-PT with Sm doping. (**A**) PFM OP amplitude images of PMN-29PT doped with 0 to 3% Sm. The right-hand insets show additional PFM images highlighting selected features of the domain structure, such as the presence of nanodomains (arrows denoted as "nanodomains") and lamellar-like domains (arrow denoted as "lamellas"). The yellow and white circles in the PFM images of the 1 and 2% Sm-doped samples indicate the lower and upper size limit of the observed nanodomains, respectively, while the blue circles highlight the lamellar domains in 2.5%- and 3%-doped samples. a.u., arbitrary units. (**B**) Cu-Kα1 XRD patterns of PMN-29PT doped with 0 to 3% Sm, highlighting the {200} peak family. XRD patterns of 3% Sm-doped PMN-xPT with x = 31, 33, and 35 mol % (gray patterns) are added for comparison to illustrate the tetragonal-like (002) peak splitting. The best-fitting phase determined by Rietveld refinement (monoclinic *Cm* and tetragonal *P4mm*) is indicated on each XRD pattern. (**C**) Tetragonality c/a determined by Rietveld refinement as a function of PT content in 3% Sm-doped PMN-PT. Undoped PMN-PT and soft PZT are added for reference [data taken from (30)]. Arrows indicate the corresponding MPB compositions in the three systems. The black long-dashed line corresponds to the extrapolated extension of the c/a compositional trend for undoped PMN-PT down to lower PT contents.

(Fig. 4B), is monoclinic *Cm* (supporting XRD data and Rietveld refinement details are reported in supplementary material 7). Our previous structural analysis performed on a similar monoclinic *Cm* composition, i.e., PMN-30PT, revealed a hierarchical domain structure encompassing multiple length scales, i.e., from wedge-shaped microscale domains in hierarchy with striation-like nanodomains down to polar regions at the atomic scale (52). We also found that the polar nanostructure is characterized by diffuse boundaries between the $[110]_{pc}$ oriented dipole clusters (pc stands for pseudo-cubic), consistent with the presence of low-angle DWs. Given the similarities in the composition and (*Cm*) symmetry of the two undoped samples, it is reasonable to expect that the PMN-29PT composition analyzed in the present study would exhibit similar multiscale domain characteristics as PMN-30PT reported in (52).

At 1% Sm doping, the wedge-like domains are still present; however, in comparison with the undoped sample, they are, in average, smaller (compare 0 and 1% Sm in Fig. 4A). In addition, irregularly shaped domains can be visualized; they are mostly interconnected, have diffuse boundaries, and are sized approximately from

subhundred to few hundreds of nanometers (see yellow and white circled regions, respectively, in Fig. 4A). By increasing the Sm concentration to 2%, the likelihood of finding wedge-like domains reduces and the irregular domains prevail (Fig. 4A, 2% Sm); the nanodomain features are still observed (Fig. 4A, 2% Sm, right-hand inset).

Although both 1%- and 2%-doped samples still exhibit *Cm* symmetry like the undoped composition (Fig. 4B), PFM analysis reveals a change in the domain structure marked by the increased irregularity and large abundance of nanosized features in Sm-doped samples (right-hand insets of Fig. 4A for 1 and 2% Sm). This kind of nanosized features have been identified in a number of Pb-based relaxor systems, such as PMN-PT (59, 60), La-doped PMN-PT (61, 62), La-doped PZT (63, 64), and $Pb(Fe_{0.5}Nb_{0.5})O_3$-$BiFeO_3$ (PFN-BFO) (65). They are commonly attributed to nanopolar clusters originating from the relaxor disorder, such as the disorder introduced by charged point defects in La-doped PZT (63) or cationic charge disorder in PMN-PT (59). The presence of nanodomains with similar sizes to those observed here in 1 and 2% Sm-doped PMN-29PT has also been reported in PMN-rich relaxor compositions, such as PMN-10PT (59) and

PMN-14PT (66). Therefore, the evolution of the nanodomain structure in the Sm concentration range of 0 to 2% shows relaxor signatures and demonstrates a strong correlation with the observed enhancement of the piezoelectric response within regime I (Fig. 2 and Fig. 3). These results are consistent with the expected increased concentration of local structural heterogeneities introduced by the Sm dopant as implied from recent theoretical and experimental studies on PMN-PT ceramics and single crystals (16, 57). Furthermore, an agreement is also found with the effect of Eu doping on the domain structure of PMN-25PT ceramics where a fragmentation of the domains, resulting in the appearance of irregular nanodomains and thus denser domain structure, was observed upon increasing dopant concentration (44, 45, 67).

When the concentration of Sm is further increased from 2 to 2.5%, we can see that the domains become even more irregular and exhibit round rather than straight edges (Fig. 4A, 2.5% Sm). At this point, another type of more regular, lamellar-like domains begins to appear (Fig. 4A, 2.5% Sm, blue circles in the right-hand inset). While the first impression may be counterintuitive, this domain (ir)regularity reflects the transitional nature of the piezoelectric response (Fig. 2 and Fig. 3). Last, the lamellar domains grow in size and become the prevailing domain features in 3% Sm-doped sample (Fig. 4A, 3% Sm), although irregular patterns and residual nanodomains could still be observed (see right-hand inset for 3% Sm).

The lamellar domain structure, as observed in the 3%-doped sample, is typical for tetragonal PMN-xPT compositions, which, in the undoped system, corresponds to approximately $x \geq 35$ (52, 60, 61). The correlation between the lamellar domains and tetragonal phase in the Sm-doped PMN-PT system is supported by the $(002)_{pc}$ peak splitting and the prevalence of the tetragonal $P4mm$ phase in 2.5 and 3% Sm-doped PMN-29PT ceramics (Fig. 4B and supplementary material 7). For additional support to this correlation, we also prepared a set of ceramic samples of fixed Sm concentration (3%) but with different PT contents (namely, 31, 33, and 35 mol % PT). As seen in Fig. 4B (gray XRD patterns), these samples exhibit a clear tetragonal-like $(002)_{pc}$ splitting and are characterized by a lamellar-like domain structure [see PFM and scanning electron microscopy (SEM) images in supplementary materials 8 and 9, respectively]. The presence of tetragonal phase in PMN-29PT doped with 2.5% Sm was consistently reported in a number of other studies using either laboratory or synchrotron diffractometry (16, 29, 31, 34).

To further investigate the structural features of the tetragonal phase, we determined its tetragonality, i.e., c/a ratio. Figure 4C collects the results for the 3% Sm-doped PMN-PT compositions where the undoped PMN-PT and soft PZT c/a ratios are added for comparison. As expected, the c/a ratio in all the three systems almost linearly increase with the addition of the tetragonal PT end-member. A nearly continuous line is observed when comparing the c/a compositional trend of Sm-doped and undoped PMN-PT, supporting the simplest hypothesis that Sm doping increases the stability of the tetragonal phase for compositions with $x < 35$ where $x = 35$ is the critical (MPB) composition in the undoped system. To be noted, however, is that a small but measurable offset in the c/a ratio is observed in the 35PT composition [$c/a = 1.00801(2)$ for 3% Sm-doped and $c/a = 1.00883(2)$ for undoped composition]. Assuming that, in the undoped system, this offset would extend linearly all the way down to 29PT (represented by black dashed line in Fig. 4C), the lower c/a ratio of the 3% Sm-doped PMN-PT, relative to the extrapolated c/a trend for the undoped PMN-PT system, reveals

an additional effect of Sm doping in reducing the tetragonality, thus leading to a more pseudo-cubic lattice. This is consistent with the Sm-induced lowering of T_f closer to room temperature (see Fig. 1A, point C), meaning a closer proximity to the pseudo-cubic ergodic phase.

When the comparison of the tetragonality is made between the MPB compositions of the three systems, it is evident that the tetragonal distortion in Sm-doped PMN-PT [$c/a = 1.00284(2)$, red arrow] is notably smaller than that of undoped PMN-PT [$c/a = 1.00883(2)$, black arrow] and even an order of magnitude smaller with respect to that in soft PZT [$c/a = 1.02766(3)$, green arrow]. The small tetragonal-like distortion in morphotropic 3% Sm-doped PMN-29PT and the presence of polar nanofeatures (Fig. 4A, 3% Sm, right-hand inset) open further questions regarding the local polar structure in this sample, which is elaborated in the next step.

To understand the local structural characteristics, we further analyze the PMN-29PT with 3% Sm at the atomic scale using high-angle annular dark-field (HAADF) scanning TEM (STEM). The original HAADF STEM image is shown in Fig. 5A where the perovskite A and B sites are visualized as bigger (brighter) and smaller (darker) spots, respectively. The analysis of the B site displacements from the center of their A site perovskite cage in $[100]_{pc}$ projection is shown in Fig. 5B. The map indicates that the displacements are not uniform throughout the ~12 x 12 nm area and are rather clustered into nanoregions of similar displacement direction and magnitude of up to 25 pm. The displacement vectors within the nanoregions exhibit substantial variations, although gradually and consistently between the $[001]_{pc}$ and $[011]_{pc}$ directions (or $[111]_{pc}$ in real space; see squared areas and arrows in Fig. 5B). This nanoscale features could influence the changing of the long-range crystal symmetry, affecting the varying domain structure from lamellar to irregular, as indicated by PFM (see Fig. 4A) and SEM imaging (supplementary material 9). The polar clusters in this 3% Sm-doped PMN-29PT composition appear similar in nature to those found earlier in undoped PMN-30PT (52), although the domain structure is different, reflecting the effect of Sm doping on the development of lamellar domains (which are not present in undoped PMN-30PT).

As a summary of the structural part, combined XRD and PFM analysis confirms that Sm induces a tetragonal phase in the otherwise monoclinic (Cm) PMN-29PT with partially lamellar domains when approaching the highest 3% dopant concentration (consistent with dielectric analysis, i.e., arrow A in Fig. 1A). It must be stressed, however, that, on an average scale (XRD), the lattice distortion of the tetragonal cell deviates little from pseudo-cubic (corresponding to small c/a ratio). This further agrees with the atomic-scale picture, obtained by STEM, where off-centric atom displacements do not exclusively adopt the $[001]_{pc}$ tetragonal directions (which is, on average, the major distortion) but vary locally between the tetragonal and rhombohedral-like or monoclinic symmetries (projected $[011]_{pc}$ direction). Exactly the same picture was extracted from diffraction data by Zhao *et al.* (29) who reported on the dissimilarities between the average (tetragonal) structure and local (monoclinic-like) distortions in 2.5% Sm-doped PMN-29.5PT. Such deviations of local symmetry from the average structure is typical for relaxor-based materials (14) and is consistent with the fine nanodomain structure (Fig. 4A) and frequency-dispersed permittivity maximum (Fig. 1, B and C) observed in 3% Sm-doped PMN-29PT. At this point, it is also important to note that the nonlinear piezoelectric response of the 3% Sm composition shows, on average, RL-like
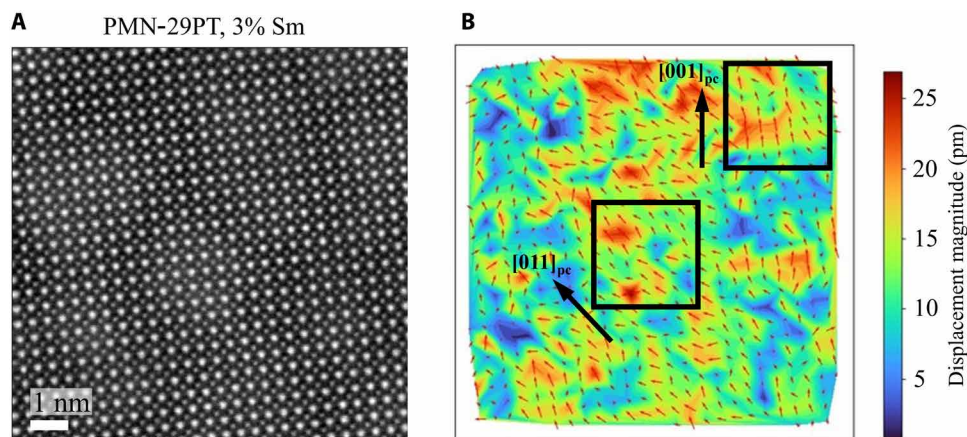
Fig. 5. Atomic structure of PMN-29PT doped with 3% Sm. (**A**) HAADF STEM image in $[100]_{pc}$ zone with bigger/brighter A site atomic columns and smaller/lighter B site atomic columns. (**B**) Vector map of B site displacements away from the center of the A site perovskite sublattice. Arrows mark the direction and magnitude (arrow length) of the displacements, and the contours additionally mark their magnitude. The squares and arrows indicate local displacement regions with preferred $[001]_{pc}$ and $[011]_{pc}$ orientations.

characteristics; however, residual features of the largely hysteretic response, typical for compositions with 0 to 2% Sm, are still observed (e.g., the experimental hysteresis of 3% Sm sample is still 36% larger than that calculated using RL equations; see Fig. 3C). This indicates that the ultrahigh response of 3% Sm-doped PMN-29PT is likely attributed to a combination of at least two main factors, i.e., the presence of the tetragonal phase and the relaxor-like structural features. To be emphasized at this point is that both the tetragonality and increased relaxor disorder induced by the Sm doping could be explained by considering the local structural consequences of the replacement of the Pb^{2+} cations with the smaller Sm^{3+} cations at the A sites of PMN-PT (*19*). First-principles calculations confirmed the tendency of a strong local tetragonal distortion around the A site–incorporated Sm^{3+} cations. The predicted local tetragonal distortion was subsequently confirmed by HAADF STEM imaging of Sm-doped PMN-PT single crystals (*57*), potentially explaining the origin of the relaxor disorder introduced by the dopant.

The comparison of the domain-structure evolution (Fig. 4A) with the piezoelectric response measured at room temperature (Fig. 2) reveals further details. Specifically, it appears as the transition from the superlinear d'_{33}–electric-field dependency, related to the dynamic contribution of low-angle DWs under field in undoped PMN-29PT, to the sublinear trend above 2% Sm (see Fig. 2A) is intimately linked to the appearance of lamellar domains and tetragonal phase (Fig. 4, A and B). The piezoelectric transition has thus origins in the qualitative change in the DW contribution by Sm doping with additional contributions that may arise from interface boundary dynamics characteristic for MPB compositions (*49*).

Deconvolution of the nonlinear piezoelectric response

We come back to the analysis of the piezoelectric response and further verify if the RL-like behavior, apparently induced by Sm doping in PMN-29PT (Fig. 3), is an effect associated with the transition from the monoclinic *Cm* to the tetragonal *P4mm* phase as suggested by PFM and XRD analysis. For this purpose, we used a sample with a fixed Sm concentration and verify if a transition to the RL-like behavior can be induced thermally by approaching T_{tetr} (see Fig. 1B),

instead of doping with Sm as already suggested by combined piezoelectric and structural data. We chose PMN-29PT with 2% Sm because this composition shows a clear non-RL piezoelectric behavior at room temperature (i.e., at the limit of regimes I and II; Fig. 3) and has a relatively low T_{tetr} (45°C; Fig. 1C). The latter should minimize possible complications in the interpretation of the results related to thermal effects.

Figure 6A combines the results of the simultaneous dynamic piezoelectric and dielectric measurements (top) and isothermal piezoelectric harmonic analysis (bottom). The two datasets are connected with a vertical red line indicating T_{tetr} (extracted from the dielectric data; Fig. 1C). The nature of this transition was confirmed by the appearance of tetragonal-like XRD peak splitting and lamellar domains (PFM) during heating above T_{tetr} (supplementary material 10). A large enhancement in the piezoelectric d'_{33} coefficient is observed with temperature, peaking at T_{tetr} (45°C) to a value of ~1440 pm/V (Fig. 6A, full curve). The other anomaly in the dynamic d'_{33} curve is an abrupt drop of the coefficient between 65° and 70°C, which is near T_f and thus likely related to a partial depoling of the sample.

First and third harmonic isothermal data confirm the transition to an RL-like nonlinear response as T_{tetr} is approached (see $\frac{\Delta d''_{33}}{\Delta d'_{33}}$ and δ_3 evolution toward the RL line in Fig. 6A, bottom plot). Therefore, we can firmly conclude that the RL-like nonlinear response that was found to emerge in PMN-29PT by Sm doping (Fig. 3) is merely a secondary effect of T_{tetr} shifting closer to room temperature. The generality of this relationship is further demonstrated in Fig. 6B by plotting the temperature dependence of δ_3 for all the PMN-29PT compositions (the original E_0-dependent data are shown in supplementary material 11). In all the cases, the δ_3 values asymptotically approach the RL-predicted value of −90° as the samples are heated toward and above their respective T_{tetr} (indicated by color-coded vertical bands in Fig. 6B). The Sm dopant itself cannot be responsible for this effect because the same transition is observed by annealing undoped PMN-PT (black curve in Fig. 6B). This claim is also supported by the compositionally induced RL-like piezoelectric behavior previously observed at the M-to-T MPB in undoped
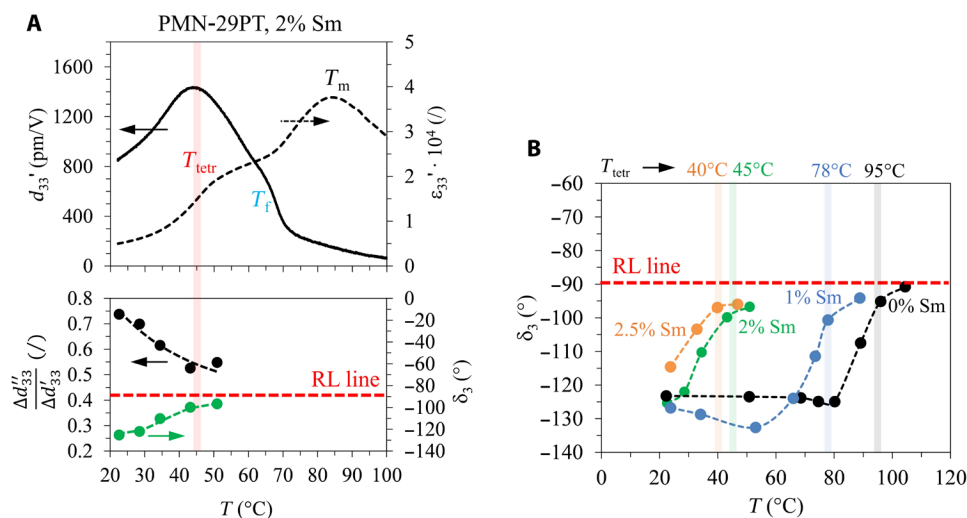
Fig. 6. Temperature-dependent dielectric and piezoelectric response of PMN-29PT doped with 0 to 3% Sm. (**A**) Temperature dependence of dielectric permittivity ε' and piezoelectric d'_{33} coefficient (top plot; dynamic measurements) and piezoelectric harmonic responses (bottom plot; isothermal measurements) of PMN-29PT ceramics doped with 2% Sm (data acquired during heating). The bottom plot includes the first harmonic ratio of the hysteretic-to-nonlinear fractional contributions, $\frac{\Delta d''_{33}}{\Delta d'_{33}}$, and the third harmonic phase angle, δ_3 (the latter is shown for $E_0 = 0.13$ kV/cm, which is the maximum field used for measurements at the highest temperature of 51°C). The red dashed line indicates the $\frac{\Delta d''_{33}}{\Delta d'_{33}}$ and δ_3 values corresponding to RL. (**B**) Third harmonic phase angle δ_3 (for $E_0 = 0.13$ kV/cm) plotted as a function of temperature for PMN-29PT doped with 0 to 3% Sm. The RL line is added as a reference. The colored vertical bands indicate the tetragonal-phase transition temperature T_{tetr} corresponding to different Sm concentrations (also see Fig. 1C).

PMN-PT and soft PZT (*30*). The underlying mechanism could be associated with an increased disorder induced by the multiple phase coexistence at the MPB. For example, the multiple and thus randomized polarization and strain states resulting from such a coexistence could be reflected macroscopically in a response that is closer to RL [which assumes perfectly random pinning potential (*32*)].

On the basis of the identified relationship between the RL-like response and proximity to the tetragonal phase, we can now separate the different linear and nonlinear contributions from the total measured d'_{33} coefficient. Figure 7 (A and B) shows the extracted R (d_{33}^{init}) and IR (α^*) coefficients for the undoped and Sm-doped PMN-29PT compositions plotted as a function of the proximity to the tetragonal-phase transition (where $T - T_{tetr} = 0$°C represents the point of the tetragonal phase transition). Two temperature regions can be approximately separated, which are defined here as pretransitional (green) and transitional (red) region. Using the onset of the α^* peak as the criterion (Fig. 7B), the crossover between the two regions can be set at ~15°C away from T_{tetr} (i.e., at $T - T_{tetr} \sim -15$°C). This is in excellent agreement with the crossover between the nonlinear regimes I and II determined from the room-temperature piezoelectric data, which was attributed to the shift of T_{tetr} closer to room temperature (Fig. 3A, see upper horizontal axis). Therefore, the analysis in Fig. 7 (A and B) allows us to efficiently separate the transitional and pretransitional contributions into linear and nonlinear components. While the major enhancement is observed within approximately ±15°C window around the phase transition (see α^* peaks in Fig. 7B), we still have to note that the transitional effects can extend more broadly, albeit the effect on properties becomes progressively minor (*68*). For example, the pretransitional enhancement (green region in Fig. 7A) could still be part of the enhancement related to the proximity to the tetragonal phase but extends more deeply away from T_{tetr}.

In the transitional (red) region, a peak is observed in both d_{33}^{init} (Fig. 7A) and α^* (Fig. 7B), whose magnitude, on average, increases with Sm addition (noted with the two red arrows in Fig. 7, A and B). In contrast to this transitional enhancement, a completely different behavior is observed in the pretransitional (green) region. Here, α^* is barely affected by the addition of Sm (see green arrow in Fig. 7B), while a much larger enhancement is observed in d_{33}^{init} as the concentration is increased from 0 to 2% (see green arrow in Fig. 7A). It can be thus concluded that α^* is mostly affected by the close proximity to the tetragonal-phase transition (red arrow in Fig. 7B). This is consistent with the compositional trend discussed earlier where it was shown that α^* is strongly enhanced only above 2% Sm concentration limit (see, e.g., inset of Fig. 2B), i.e., the point above which T_{tetr} is shifted to within ~15°C proximity to room temperature (see upper horizontal axis in Fig. 3A). If we consider the commonly accepted correlation between the R and IR nonlattice (e.g., DW) contributions, convoluted in the d_{33}^{init} and α^* coefficients, respectively (*31*), we can assume that the total nonlattice contributions, meaning R and IR responses to field, are mostly enhanced in the narrow transitional region where the tetragonality sets in. As a consequence, this reasoning implies that most large pretransitional enhancement in d_{33}^{init} likely originates from a lattice-like response to electric field.

In the final step, we combine the data shown in Fig. 7 (A and B) to construct cumulatively the individual contributions to the large piezoelectric response of PMN-29PT with 2.5% Sm, i.e., the ceramic composition extensively discussed in the literature (*16, 19, 31, 34*). Figure 7C shows the field-dependent piezoelectric response separated into linear (bright variants of red and green) and nonlinear (dark variants of red and green) components where each of these components are further separated into pretransitional (green color variants) and transitional (red color variants) contributions. It is clear from this analysis that most of the ultrahigh piezoelectric response, i.e., 89% of
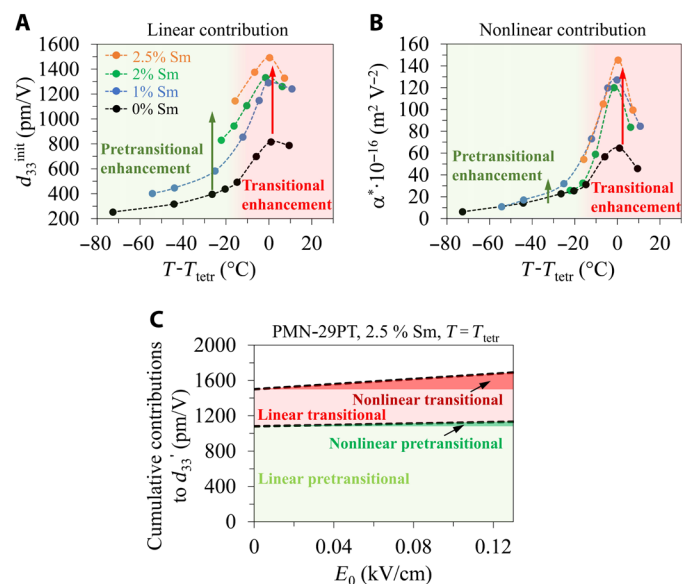
Fig. 7. Deconvolution of the piezoelectric response of Sm-doped PMN-PT. (**A**) Reversible linear d_{33}^{init} and (**B**) irreversible nonlinear α^* Rayleigh coefficients as a function of temperature (relative to T_{tetr}) shown for undoped PMN-29PT and doped with 1, 2, and 2.5% Sm (data acquired during heating). For comparison, α^* coefficients measured at $E_0 = 0.13$ kV/cm are presented. The green and red regions indicate the pretransitional and transitional regions, respectively, which were separated based on trends of the two coefficients in terms of temperature and Sm concentration (see text for details). The green and red arrows indicate the enhancement of d_{33}^{init} and α^* with increasing Sm concentration in the respective regions. (**C**) Cumulative contributions to the field-dependent piezoelectric response of PMN-29PT with 2.5% Sm at $T = T_{tetr} = 40°C$ as extracted from the data shown in (A) and (B). The total response was deconvoluted into linear (d_{33}^{init}) and nonlinear (α^*) contributions, each additionally separated into pretransitional and transitional contributions.

the total coefficient (measured at $E_0 = 0.13$ kV/cm; see Fig. 7C), originate from linear (field-independent) contributions (sum of bright green and bright red areas in Fig. 7C). Most of this linear response is pretransitional (bright green area), accounting for 64% (i.e., $\sim \frac{2}{3}$) of the total coefficient. On the other hand, transitional contributions, enhanced in the very close proximity (±15°C) to the tetragonal phase, are also important as they contribute up to 33% (i.e., $\sim \frac{1}{3}$) of the total response (sum of bright red and dark red areas in Fig. 7C).

DISCUSSION
On the basis of the analysis presented in the previous section and using the available literature data, we are now able to construct a coherent mechanistic picture describing the ultrahigh piezoelectric response of Sm-doped PMN-29PT ceramics. Recent in situ XRD studies by Zhao *et al.* (*29*) on PMN-29.5PT doped with 2.5% Sm suggested that the large piezoelectric activity of these ceramics originates from polarization rotation, which is facilitated by the presence of local thermally activated monoclinic clusters, distorted approximately along <111>$_{pc}$, that can easily rotate toward the average tetragonal <001>$_{pc}$ directions (*29*). This picture is consistent with our STEM structural analysis (see Fig. 5), suggesting that the large linear pretransitional (lattice) response, contributing to $\sim \frac{2}{3}$ of

the total piezoelectricity (bright green area in Fig. 7C), together with the lattice contribution embedded in the linear transitional response (part of bright red area in Fig. 7C), is likely related to a field-induced polarization rotation of the local polar clusters. Although different from the classical polarization rotation discussed in the frame of long-range symmetries typically in monodomain single crystals (*23–25*), we should consider that, in disordered relaxor ferroelectrics, the local symmetry could play an important role in the rotation mechanism as suggested by Zhao *et al.* (*29*). Such rotations should become progressively easier as the transition to the tetragonal phase is approached, which is supported by the peak in the d_{33}^{init} coefficient (Fig. 7A, red area), but could also persist away from the tetragonal phase, potentially explaining why the linear pretransitional contribution extends in a broad temperature range, i.e., deeply below T_{tetr} (Fig. 7A, green area). In support of this mechanism, we compare in supplementary material 12 the temperature-dependent dielectric behavior of undoped and 3% Sm-doped PMN-29PT sample, which, at cryogenic temperatures, converges to similar ε' values. These results suggest a thermally activated process, in agreement with Zhao *et al.* (*29*) who found that the local monoclinic clusters are temperature-induced. Nevertheless, we have to note that the impact of the reduced amount of pinning centers (oxygen vacancies) by Sm^{3+} donor doping and its possible role in the facilitated polarization rotation, as proposed by Li *et al.* (*31*), cannot be ruled out despite the lack of supporting evidences.

The other essential contribution, accounting for $\sim \frac{1}{3}$ of the total piezoelectricity, arises at a very close proximity (~15°C) to the tetragonal-phase transition; hence, we labeled it here as transitional enhancement (red color variants in Fig. 7C). Considering that a large extent of this contribution is of nonlattice origin, the most reasonable mechanisms are either domain wall and/or interface-boundary dynamics, which are known to be maximized at the MPB (*30*). It has to be emphasized, however, that this transitional enhancement is dependent on the Sm concentration (red arrow in Fig. 7B), meaning that the Sm-induced shift of the MPB to lower PT content (point A in Fig. 1A) and the associated MPB enhancement cannot be used as the single argument and thus likely combines with other mechanism(s). For the sake of the simplest analysis, two possibilities can be envisioned. The first possibility is a combined effect of MPB (close proximity to the tetragonal phase) and enhanced relaxor behavior introduced by Sm doping (equivalent of combining points A and B in Fig. 1A). An experimental indication supporting this scenario is the piezoelectric behavior discussed earlier for the concentration range of 0 to 2% Sm in which the relaxor-related hysteretic and anhysteretic contributions (green areas in Fig. 3, A and B) were found to increase with increasing Sm concentration. Currently, there are no arguments to exclude the presence of such a mechanism in the MPB composition. From the structural point of view, such nonlattice mechanism would be tightly linked to the complex microscale-to-nanoscale domain structure, dissimilar local and average symmetries, and local polar features arising in the MPB composition with strong relaxor character, as demonstrated here for PMN-29PT doped with 3% Sm. In this context, the local polar features could play a dual role in that they contribute to both polarization rotation and extrinsic effects; nevertheless, additional systematic investigations would be required to support this hypothesis. The second possibility is a combined effect of MPB and

softening related to Sm^{3+} donor doping on Pb^{2+} sites, which is known to result in increased nonlattice (e.g., DW) contributions (*31*). The softening effect of Sm dopant is, in our case, identified by several features, i.e., increased piezoelectric coefficient (Fig. 2A), increased domain wall contribution (Fig. 2B), and decreased coercive field (supplementary material 3) by Sm doping. From the presented data, however, the softening mechanism alone cannot explain the totality of our results. Similarly, the explanation using softening is also inconsistent with the different piezoelectric coefficients reported for PMN-PT ceramics doped with the same concentration (2.5%) but different rare-earth dopants, i.e., La, Nd, and Sm (*19*); having the same trivalent state, all of these dopants should, in principle, result in the same donor-charge compensation. To some extent, both scenarios, i.e., enhanced relaxor disorder and softening effect induced by Sm doping, may have a role. The large IR nonlinear coefficient α^* (maximum of 145×10^{-16} m^2 V^{-2}; see Fig. 7B), which is at least an order of magnitude higher than that reported for conventional soft PZT [in the range of 2×10^{-16} to 15×10^{-16} m^2 V^{-2} (*30*, *52*)], may be understood in terms of the triple effect of Sm doping in enhancing the morphotropic (and polymorphic), relaxor, and defect (donor doping–related) disorder.

Another point to consider is the decreased T_f by Sm doping (points C in Fig. 1A), which could also contribute to the large piezoelectric coefficient [see, e.g., (*69*)]. The effect of ergodicity in PMN-PT doped with 3% Sm with the lowest T_f (~43°C) is also reflected in the slanted shape of the P-E hysteresis loop and small negative strain observed in the strain-field loops (supplementary material 3), as also observed in other studies (*37*, *38*). The effect of lowered T_f by Sm doping, however, is weaker than that of the tetragonal phase transition as supported by the major d'_{33} peak observed at T_{tetr} in the dynamic measurements (Fig. 6A). This is consistent with the discussion on PMN-PT ceramics made by Li *et al.* (*16*) using Ca as a dopant, instead of Sm, and with a recent study on Sm-doped PZN-PT single crystals (*70*).

In summary, the idea of the presented study was to use a combination of nonlinear harmonic piezoelectric measurements and structural analysis over multiple scales to clarify the origins of the ultrahigh piezoelectric response of Sm-doped PMN-PT ceramics. Harmonic analysis on PMN-29PT doped with 0 to 3% Sm revealed a previously unreported transition in the nonlinear response at 2 to 2.5% Sm, showing a good correlation with evolution of the domain structure. The transition was linked to the appearance of an average tetragonal phase with low tetragonality ($c/a \sim 1.003$). The identification of this transition made it possible to further deconvolute the total piezoelectric coefficient into individual contributions. It was found that the major contribution accounts for at least $\sim \frac{2}{3}$ of the total response and is most likely associated with the polarization rotation mechanism related to the presence of local polar clusters of relaxor origins. This picture was already proposed by recent in situ structural studies and found a good agreement with the atomic-scale structural analysis presented in our study. The other mechanism, contributing to $\sim \frac{1}{3}$ of the ultrahigh piezoelectric coefficient, is mostly related to nonlattice contributions, such as domain wall or interface-boundary dynamics, which are tightly linked to the secondary effect of Sm doping in inducing a tetragonal distortion in the material. We found, however, that this MPB-like enhancement of the nonlattice response is likely affected by the increased relaxor disorder and/or donor doping (softening) effects, both induced by

Sm doping as well. Our results emphasize that, to some degree, the previously proposed explanations are all valid; however, they also point to the intricate and multiple effects of Sm doping in PMN-PT. The key result of our study is thus the confirmation that the ultrahigh piezoelectricity of Sm-doped PMN-PT ceramics cannot be simply explained by a unified, single mechanism, as implied by recent studies, but is rather a complex combination of multiple and mutually correlated mechanisms.

MATERIALS AND METHODS
Ceramic synthesis
Ceramic samples with nominal composition $Pb_{(1-3/2y)}Sm_y[(Mg_{1/3}Nb_{2/3})_{1-x}Ti_x]O_3$ were prepared by conventional solid-state synthesis using the columbite method. Two series of compositions were prepared. In the first series, the Ti concentration was fixed ($x = 0.29$) and the Sm concentration was varied ($y = 0$, 0.01, 0.02, 0.025, and 0.03). In the second series, the Sm concentration was fixed ($y = 0.03$) and the Ti concentration was varied ($x = 0.25$, 0.27, 0.31, 0.33, and 0.35). All the compositions were prepared using 0.5 mol % excess PbO.

The columbite $MgNb_2O_6$ was synthesized from a mixture of $4MgCO_3 \cdot Mg(OH)_2 \cdot 4H_2O$ (Alfa Aesar, 100%) and Nb_2O_5 (Sigma-Aldrich, 99.9%) using the MgO component in 4 mol % excess. Approximately 150 g of this mixture were placed into a 500-ml polyethylene vial together with 1300 g of yttria-stabilized zirconia (YSZ) milling balls with a diameter of 3 mm (Tosoh, Japan) and homogenized in isopropanol using attrition milling (Netzsch, Germany) for 3 hours at 500 min^{-1} of rotational frequency. The homogenized mixture was then dried overnight at 105°C and lastly calcined at 1150°C for 4 hours using 5°C/min of heating and cooling rates. After calcination, the powder was again attrition milled using the same conditions as already described.

The columbite powder together with the rest of the components, i.e., PbO (Alfa Aesar, 99.9%), TiO_2 (Alfa Aesar, 99.8%), and Sm_2O_3 (Alfa Aesar, 99.9%), was homogenized in an appropriate stoichiometry, as explained at the beginning of this section, using planetary milling (Retsch PM400, Germany) for 2 hours at 200 min^{-1} of rotational frequency. Planetary milling was performed in isopropanol using ~150 g of powder, 650 g of 3-mm YSZ milling balls, and a 500-ml YSZ vial. After drying, the powders were calcined two times in closed alumina crucibles at 850°C for 2 hours using 5°C/min of heating and cooling rates. Each calcination was followed by milling of the powder. After the first calcination, the powders were milled in a planetary mill using the same conditions as already described. Milling after the second calcination was performed in an attritor, again, using the same conditions as explained so far, followed by overnight drying of the powder at 105°C.

The calcined and dried powders were pressed into pellets at 300 MPa of isostatic pressure (Autoclave Engineers, United States). The resulting cylindrical pellets of dimensions 8 mm in diameter and ~7 mm in thickness were lastly sintered for 16 hours at different temperatures depending on the Sm concentration, i.e., at 1200°C ($y = 0$, 0.01, and 0.02), 1220°C ($y = 0.025$), or 1240°C ($y = 0.03$) using 5°C/min of heating and cooling rates. The sintering was performed in closed alumina crucible by immersing two pellets in ~5 g of packing powder consisting of $PbZrO_3$ with added 2 mol % PbO powder in excess.

Structural characterization

Room-temperature powder XRD data were collected using two diffractometers, i.e., Rigaku MiniFlex 600-C (Rigaku, Tokyo, Japan) and PANalytical X'Pert Pro (Malvern Panalytical, Malvern, UK). The Rigaku MiniFlex was used in Bragg-Brentano geometry using a Cu-Kα radiation (λ = 1.5406 Å) at a Bragg angle 2θ of 10° to 120°, a step of 0.005°, and a scan speed of 0.5°/min. The instrument was operated at 40 kV and 15 mA. A Ni filter was also used on the receiving side for Cu-K$_\beta$ stripping. The PANalytical X'Pert Pro diffractometer was operated using Cu-Kα$_1$ radiation. The powder XRD data were collected in the 2θ range of 10° to 120° with a step size of 0.016° and a counting time of 300 s per step. The in situ high-temperature XRD analysis was performed using the same PANalytical X'Pert Pro powder diffractometer in a high-temperature configuration with Cu-Kα$_1$/Kα$_2$ radiation and an Anton Paar HTK-1200 oven. The measurements were performed in the 2θ range of 10° to 120° with a step size of 0.016° and a counting time of 300 s per step. The heating rate was 5°C/min, and the sample was kept for 5 min at each temperature before being measured. The structural refinements were performed with the Rietveld method using the program GSAS-II (71).

The microstructure of the sintered pellets was examined by a scanning electron microscope (JEOL JSM-7600F, Jeol Ltd., Japan) at 15 kV in backscattered electron mode. The samples were ground and fine-polished by a conventional metallographic procedure and thermally etched at 1050°C for 5 to 10 min. Grain size distribution was determined by analyzing digitalized microstructure images in Image Tool software (version 3.0, United States). Ferroelastic domains were visualized by channeling contrast in SEM backscattered mode on nonetched polished samples. Density of the ceramics was measured using pycnometry (Micromeritis AccuPyc II 1340, United States). The relative densities were calculated using the theoretical density values reported in (16).

The ferroelectric domain structure of the prepared ceramic samples was characterized by PFM using an atomic force microscope (Jupiter, Asylum Research, Santa Barbara, CA, United States) equipped with a high-voltage option for PFM imaging. Pt-coated Si tips (OMCL-AC240TM-R3, Olympus, Japan) with a radius of curvature of ~15 nm were used. The ceramic samples were attached to the AFM holders with silver paste that served as the bottom electrode. Out-of-plane (OP) PFM images were obtained using a PFM Dual ac Resonance Tracking (DART) mode by applying ac voltages with an amplitude of 1 V and a frequency of ~350 kHz between the conducting tips and the bottom electrodes. Heating experiment was performed in an atomic force microscope (Molecular Force Probe 3D, Asylum Research, Santa Barbara, CA, United States) using a Polymer heater (Asylum Research, Santa Barbara, CA, United States) in combination with a high-voltage PFM unit. OP PFM images were obtained in DART mode by applying ac voltages with an amplitude of 4 V and a frequency of ~300 kHz between the conducting tips and the bottom electrodes.

For atomic-scale structural analysis, an electrically transparent lamella was prepared using a dual focused ion beam (Helios Nanolab 650, Thermo Fisher Scientific, MA, United States). HAADF imaging using a C$_s$-corrected scanning transmission electron microscope (ARM-200 CF, JEOL Ltd., Tokyo, Japan), operated at 200 kV with a convergence angle of 24 mrad, was used to analyze the local atom displacements in the 3% Sm-doped PMN-29PT sample. The central position of each atomic column was localized by aligned image stacking and a two-dimensional Gaussian fitting procedure. The displacements of B site atoms from the center of their nearest neighbor A site atom cage were determined by Atomap 0.3.4 and Temul Toolkit software (72).

Electrical and electromechanical measurements

For electrical and electromechanical measurements, opposite surfaces of samples were covered by magnetron-sputtered Au electrodes (5 Pascal, Italy). A set of samples were poled in silicone oil at room temperature by applying 30 kV/cm of dc field for 10 min.

Temperature-dependent dielectric measurements were performed on poled samples using a custom-made setup consisting of a tube furnace, K-type thermocouple, a Hioki IM3536 LCR meter for measurements of capacitance in parallel configuration (C$_p$) and dielectric losses, and a Labview program (National Instruments, United States) for data acquisition. The data were collected at frequencies of 10^2, 10^3, 10^4, 10^5, and 10^6 Hz by heating the sample up to a maximum of 300°C with a constant heating rate of 2°C/min, followed by cooling to room temperature with the same rate.

To evaluate the relaxor behavior of the samples in terms of the Vogel-Fulcher analysis, additional broadband dielectric spectroscopy was performed on unpoled samples in the frequency range of 20 Hz to 300 MHz. To determine the complex dielectric permittivity in the 20-Hz to 1-MHz frequency range, a simple parallel-plate capacitor partially filled with the sample under test was measured. The capacitance and loss tangent were measured with a HP4824A LCR meter. The temperature was measured with a Keithley Integra 2700 multimeter and Pt-100 temperature sensor. The data were collected during heating and cooling cycles with a constant rate of 1 K/min.

Dielectric properties above 1-MHz frequency were measured by placing the samples at the end of the coaxial line. The complex reflection coefficient was measured from such a structure by using an Agilent 8714ET vector network analyzer. The complex dielectric permittivity was calculated according to the so-called multimode capacitor model. Details about the calculation model can be found in (73).

To perform the Vogel-Fulcher analysis, the permittivity peak temperatures at distinct frequencies were extracted from the datasets using the entire measured frequency range (20 Hz to 300 MHz). According to Tagantsev (74), the frequency value corresponds to the characteristic relaxation time of the material. In this particular case, the value should correspond to the edge of relaxation distribution time (from the side of longer times). The Vogel-Fulcher parameters was obtained by fitting the data according to the Vogel-Fulcher equation

$$f = f_0 \cdot e^{-\frac{E_a}{k \cdot (T_m - T_f)}} \qquad (1)$$

where T_m is the permittivity peak temperature at a given frequency, E_a is the activation energy, T_f is the Vogel-Fulcher freezing temperature, f_0 is the relaxation frequency at infinite temperature, and k is the Boltzmann constant.

Dielectric data at cryogenic temperatures were obtained using the same setup based on an HP4824A LCR meter as described earlier. A closed-cycle cryostat (Stinger, United States) was used with a cooling rate of 0.5 K/min.

P-E and strain-electric hysteresis loops were measured simultaneously using a commercial aixACCT TF 2000 analyzer at 1 Hz of frequency and a maximum applied electric field of 40 kV/cm.

Nonlinear harmonic analysis of the converse piezoelectric response was performed using a custom-made setup consisting of a fiber optic sensor for displacement measurements (MTI 2100 Fotonic Sensor, United States). For electric driving of the samples, a voltage generator (SRS DS360, United States) and a voltage amplifier (TREK 609E-6, United States) were used. Detection of the first and third harmonic signals of the piezoelectric strain was performed by two lock-in amplifiers (SR830 DSP, United States), while the piezoelectric hysteresis was acquired using an oscilloscope (Keysight InfiniiVision 1000 X-Series, United States). The settings of the driving electric field parameters, lock-in detection, and oscilloscope, alongside data acquisition, were carried out using a custom-made Labview program (National Instruments, United States). All measurements were performed at 10 Hz of driving field frequency. Additional details of the analysis are reported in (30, 52).

Temperature-dependent harmonic measurements were performed in two different experimental configurations, i.e., dynamic and isothermal. Dynamic measurements were performed by heating the sample with a constant heating rate of 2°C/min and by simultaneous acquisition of the first harmonic component of the piezoelectric and dielectric response. The applied sinusoidal electric field amplitude and frequency were 0.2 kV/cm and 90 Hz, respectively. The dielectric harmonic response was measured using the shunt resistor method and lock-in technique as explained in detail in (52). Isothermal piezoelectric harmonic analysis was performed by heating the sample at a defined temperature where the first and third piezoelectric harmonic responses were collected with two lock-in amplifiers as a function of increasing electric field amplitude using the same setup as already described.

Supplementary Materials

This PDF file includes:
Supplementary Materials 1 to 10
Figs. S1 to S17
Table S1
References

REFERENCES AND NOTES

1. M. Sadl, K. Nadaud, M. Bah, F. Levassort, U. Eckstein, N. H. Khansur, K. G. Webber, H. Ursic, Multifunctional energy storage and piezoelectric properties of 0.65Pb(Mg$_{1/3}$Nb$_{2/3}$)O$_3$–0.35PbTiO$_3$ thick films on stainless-steel substrates. *J. Phys. Energy* **4**, 024004 (2022).

2. D. Damjanovic, R. E. Newnham, Electrostrictive and piezoelectric materials for actuator applications. *J. Intell. Mater. Syst. Struct.* **3**, 190–208 (1992).

3. B. Rožič, M. Kosec, H. Uršič, J. Holc, B. Malič, Q. M. Zhang, R. Blinc, R. Pirc, Z. Kutnjak, Influence of the critical point on the electrocaloric response of relaxor ferroelectrics. *J. Appl. Phys.* **110**, 064118 (2011).

4. K. B. Kim, D. K. Hsu, B. Ahn, Y. G. Kim, D. J. Barnard, Fabrication and comparison of PMN-PT single crystal, PZT and PZT-based 1-3 composite ultrasonic transducers for NDE applications. *Ultrasonics* **50**, 790–797 (2010).

5. T. Zhang, H. Liang, Z. Wang, C. Qiu, Y. B. Peng, X. Zhu, J. Li, X. Ge, J. Xu, X. Huang, J. Tong, J. Ou-Yang, X. Yang, F. Li, B. Zhu, Piezoelectric ultrasound energy–harvesting device for deep brain stimulation and analgesia applications. *Sci. Adv.* **8**, eabk0159 (2022).

6. C. Qiu, B. Wang, N. Zhang, S. Zhang, J. Liu, D. Walker, Y. Wang, H. Tian, T. R. Shrout, Z. Xu, L. Q. Chen, F. Li, Transparent ferroelectric crystals with ultrahigh piezoelectricity. *Nature* **577**, 350–354 (2020).

7. M. Paściak, M. Wołcyrz, A. Pietraszko, Interpretation of the diffuse scattering in Pb-based relaxor ferroelectrics in terms of three-dimensional nanodomains of the <110>-directed relative interdomain atomic shifts. *Phys. Rev. B* **76**, 014117 (2007).

8. J. Hlinka, Do we need the ether of polar nanoregions? *J. Adv. Dielectr.* **02**, 1241006 (2012).

9. A. Bosak, D. Chernyshov, S. Vakhrushev, M. Krisch, Diffuse scattering in relaxor ferroelectrics: True three-dimensional mapping, experimental artefacts and modelling. *Acta Crystallogr. Sect. A* **68**, 117–123 (2012).

10. H. Takenaka, I. Grinberg, S. Liu, A. M. Rappe, Slush-like polar structures in single-crystal relaxors. *Nature* **546**, 391–395 (2017).

11. M. J. Krogstad, P. M. Gehring, S. Rosenkranz, R. Osborn, F. Ye, Y. Liu, J. P. C. Ruff, W. Chen, J. M. Wozniak, H. Luo, O. Chmaissem, Z. G. Ye, D. Phelan, The relation of local order to material properties in relaxor ferroelectrics. *Nat. Mater.* **17**, 718–724 (2018).

12. M. Eremenko, V. Krayzman, A. Bosak, H. Y. Playford, K. W. Chapman, J. C. Woicik, B. Ravel, I. Levin, Local atomic order and hierarchical polar nanoregions in a classical relaxor ferroelectric. *Nat. Commun.* **10**, 2728 (2019).

13. A. Kumar, J. N. Baker, P. C. Bowes, M. J. Cabral, S. Zhang, E. C. Dickey, D. L. Irving, J. M. LeBeau, Atomic-resolution electron microscopy of nanoscale local structure in lead-based relaxor ferroelectrics. *Nat. Mater.* **20**, 62–67 (2021).

14. F. Li, S. Zhang, D. Damjanovic, L. Q. Chen, T. R. Shrout, Local structural heterogeneity and electromechanical responses of ferroelectrics: Learning from relaxor ferroelectrics. *Adv. Funct. Mater.* **28**, 1801504 (2018).

15. T. Rojac, Piezoelectric response of disordered lead-based relaxor ferroelectrics. *Commun. Mater.* **4**, 12 (2023).

16. F. Li, D. Lin, Z. Chen, Z. Cheng, J. Wang, C. Li, Z. Xu, Q. Huang, X. Liao, L. Q. Chen, T. R. Shrout, S. Zhang, Ultrahigh piezoelectricity in ferroelectric ceramics by design. *Nat. Mater.* **17**, 349–354 (2018).

17. J. Kelly, M. Leonard, C. Tantigate, A. Safari, Effect of composition on the electromechanical properties of (1-x)Pb(Mg$_{1/3}$Nb$_{1/3}$)O$_3$-xPbTiO$_3$ ceramics. *J. Am. Ceram. Soc.* **80**, 957–964 (1997).

18. S. E. Park, T. R. Shrout, Ultrahigh strain and piezoelectric behavior in relaxor based ferroelectric single crystals. *J. Appl. Phys.* **82**, 1804–1811 (1997).

19. C. Li, B. Xu, D. Lin, S. Zhang, L. Bellaiche, T. R. Shrout, F. Li, Atomic-scale origin of ultrahigh piezoelectricity in samarium-doped PMN-PT ceramics. *Phys. Rev. B* **101**, 140102 (2020).

20. Q. Guo, F. Lintao Hou, F. Li, P. Xia, H. Wang, H. Hao, H. L. Sun, S. Zhang, Investigation of dielectric and piezoelectric properties in aliovalent Eu^{3+}-modified Pb(Mg$_{1/3}$Nb$_{2/3}$) O$_3$-PbTiO$_3$ ceramics. *J. Am. Ceram. Soc.* **102**, 7428–7435 (2019).

21. L. Bian, Q. Wang, X. Qi, K. Li, S. He, G. Jiang, Y. Yang, B. Yang, Improved electromechanical properties of Pb(Ni$_{1/3}$Nb$_{2/3}$)O$_3$–PbZrO$_3$–PbTiO$_3$ ferroelectric ceramics via Sm-modification. *Ceram. Int.* **50**, 5739–5745 (2024).

22. G. G. Peng, D. Y. Zheng, S. M. Hu, H. Zhao, C. Cheng, J. Zhang, Effects of rare-earth Sm$_2$O$_3$ addition on relaxation behavior and electric properties of 0.5PNN-0.5PZT ceramics. *J. Mater. Sci. Mater. Electron.* **27**, 5509–5516 (2016).

23. H. Fu, R. E. Cohen, Polarization rotation mechanism for ultrahigh electromechanical response in single-crystal piezoelectrics. *Nature* **403**, 281–283 (2000).

24. D. Damjanovic, Contributions to the piezoelectric effect in ferroelectric single crystals and ceramics. *J. Am. Ceram. Soc.* **88**, 2663–2676 (2005).

25. M. Iwata, Y. Ishibashi, Phenomenological theory of morphotropic phase boundary with monoclinic phase in solid-solution systems of perovskite-type oxide ferroelectrics. *Jpn. J. Appl. Phys.* **44**, 3095–3098 (2005).

26. F. Li, S. Zhang, T. Yang, Z. Xu, N. Zhang, G. Liu, J. Wang, J. Wang, Z. Cheng, Z. G. Ye, J. Luo, T. R. Shrout, L. Q. Chen, The origin of ultrahigh piezoelectricity in relaxor-ferroelectric solid solution crystals. *Nat. Commun.* **7**, 13807 (2016).

27. P. M. Shepley, L. A. Stoica, Y. Li, G. Burnell, A. J. Bell, Effects of poling and crystallinity on the dielectric properties of Pb(In$_{1/2}$Nb$_{1/2}$)O$_3$-Pb(Mg$_{1/3}$Nb$_{2/3}$)O$_3$-PbTiO$_3$ at cryogenic temperatures. *Sci. Rep.* **9**, 9 (2019).

28. A. J. Bell, P. M. Shepley, Y. Li, Domain wall contributions to piezoelectricity in relaxor-lead titanate single crystals. *Acta Mater.* **195**, 292–303 (2020).

29. C. Zhao, F. Li, S. Zhang, S. Li, J. L. Jones, Mechanisms underpinning the ultrahigh piezoelectricity in Sm-doped 0.705Pb(Mg$_{1/3}$Nb$_{2/3}$)O$_3$-0.295PbTiO$_3$: Temperature-induced metastable local structure and field-induced polarization rotation. *J. Appl. Phys.* **126**, 075101 (2019).

30. M. Otonicar, M. Dragomir, T. Rojac, Dynamics of domain walls in ferroelectrics and relaxors. *J. Am. Ceram. Soc.* **105**, 6479–6507 (2022).

31. Y. Li, M. Borbely, A. Bell, The influence of oxygen vacancies on piezoelectricity in samarium-doped Pb(Mg$_{1/3}$Nb$_{2/3}$)O$_3$-PbTiO$_3$ ceramics. *J. Am. Ceram. Soc.* **104**, 2678–2688 (2021).

32. D. Damjanovic, Ferroelectric, dielectric and piezoelectric properties of ferroelectric thin films and ceramics. *Rep. Prog. Phys.* **61**, 1267–1324 (1998).

33. A. Bradeško, M. Vrabelj, L. Fulanović, Š. Svirskas, M. Ivanov, R. Katiliūte, D. Jablonskas, M. Šimėnas, G. Usevičius, B. Malič, J. Banys, T. Rojac, Implications of acceptor doping in the polarization and electrocaloric response of 0.9Pb(Mg$_{1/3}$Nb$_{2/3}$)O$_3$-0.1PbTiO$_3$ relaxor ferroelectric ceramics. *J. Mater. Chem. C* **9**, 3204–3214 (2021).

34. N. Kumar, A. Mishra, A. De, U. Shankar, R. Ranjan, Factors contributing to the local polar-structural heterogeneity and ultrahigh piezoelectricity in Sm-modified Pb(Mg$_{1/3}$Nb$_{2/3}$)O$_3$-PbTiO$_3$. *J. Phys. D Appl. Phys.* **53**, 165302 (2020).

35. P. Mikhail, J. Hulliger, Sm^{2+} in oxide lattices: An unexplored chapter of crystal chemistry. *Comments Inorg. Chem.* **21**, 263–283 (1999).

36. B. Noheda, D. E. Cox, G. Shirane, J. Gao, Z. G. Ye, Phase diagram of the ferroelectric relaxor (1-x)PbMg$_{1/3}$Nb$_{2/3}$O$_3$-xPbTiO$_3$. *Phys. Rev. B* **66**, 054104 (2002).

37. H. Jia, J. Mi, Z. Li, L. Wang, Improved dielectric and piezoelectric properties of Sm-doped Pb(Mg$_{1/3}$Nb$_{2/3}$)O$_3$–Pb(Zn$_{1/3}$Nb$_{2/3}$)-PbTiO$_3$ ternary ferroelectric ceramics. *Ceram. Int.* **48**, 14761–14766 (2022).

38. H. Jia, S. Yang, W. Zhu, F. Li, L. Wang, Improved piezoelectric properties of Pb(Mg$_{1/3}$Nb$_{2/3}$)O$_3$-PbTiO$_3$ textured ferroelectric ceramics via Sm-doping method. *J. Alloys Compd.* **881**, 160660 (2021).

39. Z. Fang, X. Tian, F. Zheng, X. Jiang, Y. Ye, Y. Qin, X. Wang, Y. Zhang, Enhanced piezoelectric properties of Sm^{3+}-modified PMN-PT ceramics and their application in energy harvesting. *Ceram. Int.* **48**, 7550–7556 (2022).

40. C. Singh, A. Kumar, Improved energy storage density and energy efficiency of Samarium modified PMNT electroceramic. *Ceram. Int.* **48**, 18278–18285 (2022).

41. Y. Yang, E. Sun, Z. Xu, H. Zheng, B. Yang, R. Zhang, W. Cao, Sm and Mn co-doped PMN-PT piezoelectric ceramics: Defect engineering strategy to achieve large d$_{33}$ and high Q$_m$. *J. Mater. Sci. Technol.* **137**, 143–151 (2023).

42. N. Zhong, P. H. Xiang, D. Z. Sun, X. L. Dong, Effect of rare earth additives on the microstructure and dielectric properties of 0.67Pb(Mg$_{1/3}$Nb$_{2/3}$)O$_3$-0. 33PbTiO$_3$ ceramics. *Mater. Sci. Eng. B* **116**, 140–145 (2005).

43. Y. Huang, L. Zhang, W. Shi, Q. Hu, V. Shur, X. Wei, L. Jin, Ferroelectric-to-relaxor transition and ultrahigh electrostrictive effect in Sm^{3+}-doped Pb(Mg$_{1/3}$Nb$_{2/3}$)O$_3$-PbTiO$_3$ ferroelectric ceramics. *J. Mater. Sci. Technol.* **165**, 75–84 (2023).

44. Y. Zhou, K. Zhao, W. Ruan, J. Zeng, L. Zheng, G. Li, Electric field-induced light scattering in Eu-doped PMN-PT transparent ceramics. *J. Am. Ceram. Soc.* **99**, 3993–3999 (2016).

45. K. Li, E. Sun, Y. Zhang, Z. Song, X. Qi, Y. Sun, J. Li, B. Yang, J. Liu, W. Cao, High piezoelectricity of Eu^{3+}-doped Pb(Mg$_{1/3}$Nb$_{2/3}$)O$_3$-0.25PbTiO$_3$ transparent ceramics. *J. Mater. Chem. C* **9**, 2426–2436 (2021).

46. Y. Yang, K. Zhu, E. Sun, P. Liu, R. Zhang, W. Cao, Ultrabroad-bandwidth ultrasonic transducer based on Sm-doped PMN-PT ceramic/epoxy 1–3 composite. *Sens. Actuat. A Phys.* **346**, 113873 (2022).

47. Z. Zhang, M. Su, F. Li, R. Liu, R. Cai, G. Li, Q. Jiang, H. Zhong, T. R. Shrout, S. Zhang, H. Zheng, W. Qiu, New Sm-PMN-PT ceramic-based 2-D array for low-intensity ultrasound therapy application. *IEEE Trans. Ultrason. Ferroelectr. Freq. Control* **67**, 2085–2094 (2020).

48. D. Damjanovic, M. Demartin, Contribution of the irreversible displacement of domain walls to the piezoelectric effect in barium titanate and lead zirconate titanate ceramics. *J. Phys. Condens. Matter* **9**, 4943–4953 (1997).

49. J. L. Jones, E. Aksel, G. Tutuncu, T. M. Usher, J. Chen, X. Xing, A. J. Studer, Domain wall and interphase boundary motion in a two-phase morphotropic phase boundary ferroelectric: Frequency dispersion and contribution to piezoelectric and dielectric properties. *Phys. Rev. B* **86**, 024104 (2012).

50. Q. Guo, X. Meng, F. Li, F. Xia, P. Wang, X. Gao, J. Wu, H. Sun, H. Hao, H. Liu, S. Zhang, Temperature-insensitive PMN-PZ-PT ferroelectric ceramics for actuator applications. *Acta Mater.* **211**, 116871 (2021).

51. L. M. Riemer, L. Jin, H. Uršič, M. Otoničar, T. Rojac, D. Damjanovic, Dielectric and electro-mechanic nonlinearities in perovskite oxide ferroelectrics, relaxors, and relaxor ferroelectrics. *J. Appl. Phys.* **129**, 054101 (2021).

52. M. Otoničar, A. Bradeško, L. Fulanović, T. Kos, H. Uršič, A. Benčan, M. J. Cabral, A. Henriques, J. L. Jones, L. Riemer, D. Damjanovic, G. Dražić, B. Malič, T. Rojac, Connecting the multiscale structure with macroscopic response of relaxor ferroelectrics. *Adv. Funct. Mater.* **30**, 2006823 (2020).

53. M. Otoničar, A. Bradeško, S. Salmanov, C. C. Chung, J. L. Jones, T. Rojac, Effects of poling on the electrical and electromechanical response of PMN–PT relaxor ferroelectric ceramics. *Open Ceram.* **7**, 100140 (2021).

54. Y. M. Jin, Y. U. Wang, A. G. Khachaturyan, J. F. Li, D. Viehland, Adaptive ferroelectric states in systems with low domain wall energy: Tetragonal microdomains. *J. Appl. Phys.* **94**, 3629–3640 (2003).

55. Y. Sato, T. Hirayama, Y. Ikuhara, Real-time direct observations of polarization reversal in a piezoelectric crystal: Pb(Mg$_{1/3}$Nb$_{2/3}$)O$_3$-PbTiO$_3$ studied via in situ electrical biasing transmission electron microscopy. *Phys. Rev. Lett.* **107**, 187601 (2011).

56. S. Dong, F. Guo, H. Zhou, W. Long, P. Fang, X. Li, Z. Xi, Phase structures and electrical properties of Sm doped PSN-PMN-PT ceramics. *J. Alloys Compd.* **881**, 160621 (2021).

57. F. Li, M. J. Cabral, B. Xu, Z. Cheng, E. Dickey, J. Lebeau, J. Wang, J. Luo, S. Taylor, W. Hackenberger, L. Bellaiche, Z. Xu, T. R. Shrout, S. Zhang, Giant piezoelectricity of Sm-doped Pb(Mg$_{1/3}$Nb$_{2/3}$)O$_3$-PbTiO$_3$ single crystal. *Science* **364**, 264–268 (2019).

58. M. Otonicar, H. Ursic, M. Dragomir, A. Bradesko, G. Esteves, J. L. Jones, A. Bencan, B. Malic, T. Rojac, Multiscale field-induced structure of (1-x)Pb(Mg$_{1/3}$Nb$_{2/3}$)O$_3$-xPbTiO$_3$ ceramics from combined techniques. *Acta Mater.* **154**, 14–24 (2018).

59. V. V. Shvartsman, A. L. Kholkin, Evolution of nanodomains in 0.9PbMg$_{1/3}$Nb$_{2/3}$O$_3$-0.1PbTiO$_3$ single crystals. *J. Appl. Phys.* **101**, 064108 (2007).

60. F. Bai, J. Li, D. Viehland, Domain hierarchy in annealed (001)-oriented Pb(Mg$_{1/3}$Nb$_{2/3}$)O$_3$-xPbTiO$_3$ single crystals. *Appl. Phys. Lett.* **85**, 2313–2315 (2004).

61. D. Viehland, M. C. Kim, Z. Xu, J. F. Li, Long-time present tweedlike precursors and paraelectric clusters in ferroelectrics containing strong quenched randomness. *Appl. Phys. Lett.* **67**, 2471–2473 (1995).

62. S. M. Gupta, D. Viehland, Role of charge compensation mechanism in La-modified Pb(Mg$_{1/3}$Nb$_{2/3}$)O$_3$-PbTiO$_3$ ceramics: Enhanced ordering and pyrochlore formation. *J. Appl. Phys.* **80**, 5875–5883 (1996).

63. V. V. Shvartsman, A. L. Kholkin, A. Orlova, D. Kiselev, A. A. Bogomolov, A. Sternberg, Polar nanodomains and local ferroelectric phenomena in relaxor lead lanthanum zirconate titanate ceramics. *Appl. Phys. Lett.* **86**, 202907 (2005).

64. X. Dai, Z. Xu, D. Viehland, Normal to relaxor ferroelectric transformations in lanthanum-modified tetragonal-structured lead zirconate titanate ceramics. *J. Appl. Phys.* **79**, 1021–1026 (1996).

65. U. Prah, M. Dragomir, T. Rojac, A. Benčan, R. Broughton, C. C. Chung, J. L. Jones, R. Sherbondy, G. Brennecka, H. Uršič, Strengthened relaxor behavior in (1-x)Pb(Fe$_{0.5}$Nb$_{0.5}$)O$_3$-xBiFeO$_3$. *J. Mater. Chem. C* **8**, 3452–3462 (2020).

66. V. V. Shvartsman, A. L. Kholkin, Investigation of the ferroelectric-relaxor transition in PbMg$_{1/3}$Nb$_{2/3}$O$_3$-PbTiO$_3$ ceramics by piezoresponse force microscopy. *J. Appl. Phys.* **108**, 042007 (2010).

67. K. Zhao, J. Zeng, K. Xu, H. Zeng, G. Li, Dynamic behaviors of ferroelectric domain structures in Eu-doped PMN-PT transparent ceramics studied by piezoresponse force microscopy. *J. Mater. Sci. Mater. Electron.* **31**, 15991–15995 (2020).

68. M. Budimir, D. Damjanovic, N. Setter, Piezoelectric anisotropy-phase transition relations in perovskite single crystals. *J. Appl. Phys.* **94**, 6753–6761 (2003).

69. K. Yao, C. Zhou, Q. Li, Z. Xiao, C. Yuan, J. Xu, G. Chen, G. Rao, Nonergodic–ergodic relaxor transition and enhanced piezoelectric properties in B-site complex ions substitution 0.93Bi$_{0.5}$Na$_{0.5}$TiO$_3$–0.07BaTiO$_3$ ceramics. *J. Mater. Sci. Mater. Electron.* **32**, 24308–24319 (2021).

70. H. Li, W. Liao, B. Sun, Y. Lu, X. He, Z. Xu, C. Huang, Z. Sun, T. Li, Piezoelectricity of Sm-doped Pb(Zn$_{1/3}$Nb$_{2/3}$)O$_3$–PbTiO$_3$ single crystals by enhancement of local disorder polarization. *Ceram. Int.* **49**, 8325–8330 (2023).

71. B. H. Toby, R. B. Von Dreele, GSAS-II: The genesis of a modern open-source all purpose crystallography software package. *J. Appl. Cryst.* **46**, 544–549 (2013).

72. M. Nord, P. E. Vullum, I. MacLaren, T. Tybell, R. Holmestad, Atomap: A new software tool for the automated analysis of atomic resolution images using two-dimensional Gaussian fitting. *Adv. Struct. Chem. Imaging* **3**, 9 (2017).

73. Š. Svirskas, D. Jablonskas, S. Rudys, S. Lapinskas, R. Grigalaitis, J. Banys, Broad-band measurements of dielectric permittivity in coaxial line using partially filled circular waveguide. *Rev. Sci. Instrum.* **91**, 035106 (2020).

74. A. K. Tagantsev, Vogel-Fulcher relationship for the dielectric permittivity of relaxor ferroelectrics. *Phys. Rev. Lett.* **72**, 1100–1103 (1994).

75. D. Damjanovic, Stress and frequency dependence of the direct piezoelectric effect in ferroelectric ceramics. *J. Appl. Phys.* **82**, 1788–1797 (1997).

76. D. A. Hall, Nonlinearity in piezoelectric ceramics. *J. Mater. Sci.* **36**, 4575–4601 (2001).

77. N. Bassiri-Gharb, I. Fujii, E. Hong, S. Trolier-Mckinstry, D. V. Taylor, D. Damjanovic, Domain wall contributions to the properties of piezoelectric thin films. *J. Electroceram.* **19**, 49–67 (2007).

78. P. Bintachitt, S. Jesse, D. Damjanovic, Y. Han, I. M. Reaney, S. Trolier-McKinstry, S. V. Kalinin, Collective dynamics underpins Rayleigh behavior in disordered polycrystalline ferroelectrics. *Proc. Natl. Acad. Sci. U.S.A.* **107**, 7219–7224 (2010).

79. G. Robert, D. Damjanovic, N. Setter, A. V. Turik, Preisach modeling of piezoelectric nonlinearity in ferroelectric ceramics. *J. Appl. Phys.* **89**, 5067–5074 (2001).

80. D. A. Hall, P. J. Stevenson, High field dielectric behaviour of ferroelectric ceramics. *Ferroelectrics* **228**, 139–158 (1999).

81. M. Davis, D. Damjanovic, N. Setter, Direct piezoelectric effect in relaxor-ferroelectric single crystals. *J. Appl. Phys.* **95**, 5679–5684 (2004).

82. D. Damjanovic, "Hysteresis in piezoelectric and ferroelectric materials" in *The Science of Hysteresis*, I. Mayergoyz, G. Bertotti, Eds. (Elsevier, 2006), vol. 3, pp. 337–465.

83. M. I. Morozov, D. Damjanovic, Hardening-softening transition in Fe-doped Pb(Zr,Ti)O$_3$ ceramics and evolution of the third harmonic of the polarization response. *J. Appl. Phys.* **104**, 034107 (2008).

84. X. L. Zhang, Z. X. Chen, L. E. Cross, W. A. Schulze, Dielectric and piezoelectric properties of modified lead titanate zirconate ceramics from 4.2 to 300 K. *J. Mater. Sci.* **18**, 968–972 (1983).